CMS Draft Analysis Note

The content of this note is intended for CMS internal use and distribution only

2019/08/07
Archive Hash: 820b0c4-D
Archive Date: 2019/05/09

Measurement of the top quark mass with single top events at 13 TeV

T. Aziz[1], R. Karnam[1], M. Kumar[1], S. Mitra[2], G.B. Mohanty[1], and T.Müller[2]

[1] Tata Institute of Fundamental Research
[2] Karlsruhe Institute of Technology

Abstract

A measurement of the top quark mass is performed with single top events using 35.9 fb^{-1} of proton-proton collision data collected at $\sqrt{s}$ = 13 TeV by the CMS experiment during 2016. The analysis is performed in the $\mathrm{t} \to \mathrm{bW} \to \mathrm{b}\ell\nu$ decay channel. Signal events are selected by requiring an isolated energetic muon or electron, large missing transverse momentum, and at least two hadronic jets. One of the jets is identified to originate from a bottom quark or antiquark, whereas the other results from the hadronization of a light-flavor quark within the pseudorapidity range $|\eta| \leq 4.7$. The masses of top quark and antiquark (along with their difference) are determined separately depending on the charge of the lepton in the final state. The analysis is in progress in a ”blind” way and the final result is expected soon.

1 Introduction

The top quark mass is one of the most important parameters of the standard model (SM) of particle physics. Its precise measurement is of profound importance, both for theory and experiment. It constitutes a major input to the global electroweak fits, used to verify the self-consistency of the SM. Its value is also directly related to the stability of electroweak vacuum, because among all SM particles it is the largest contributor in terms of radiative corrections to the mass and self-coupling [1] of the Higgs boson. From the experimental perspective, it provides an ideal benchmark to determine the calibration and performance of the detector as well as of reconstruction algorithms. The latest world average of the top mass [2], based on measurements performed with top pair ($\mathrm{t\bar{t}}$) events, from ATLAS, CMS, CDF and D0 collaborations, is :

$$\mathrm{m_t} = 173.34 \pm 0.27\,(\mathrm{stat}) \pm 0.71\,(\mathrm{syst})\,\mathrm{GeV} \quad (1)$$

Top quarks are produced copiously in proton-proton (pp) collisions at the Large Hadron Collider (LHC). Here, $\mathrm{t\bar{t}}$ events are dominantly produced via gluon-gluon fusion followed by quark-antiquark annihilation. A good number of single top quark events are also produced through charged-current interaction via the exchange of a W boson. Single top production, at leading order (LO) in the SM, can be realized in three modes, the *t*-channel, the tW-channel and the *s*-channel, ordered according to their cross sections. Feynman diagrams of these three production modes are shown in Figure 1. The *t*-channel is the most dominant single-top production mode in pp collisions at the LHC, with a total cross section of 217 pb calculated at next-to-leading order (NLO) with HATHORv2.1 [3, 4].

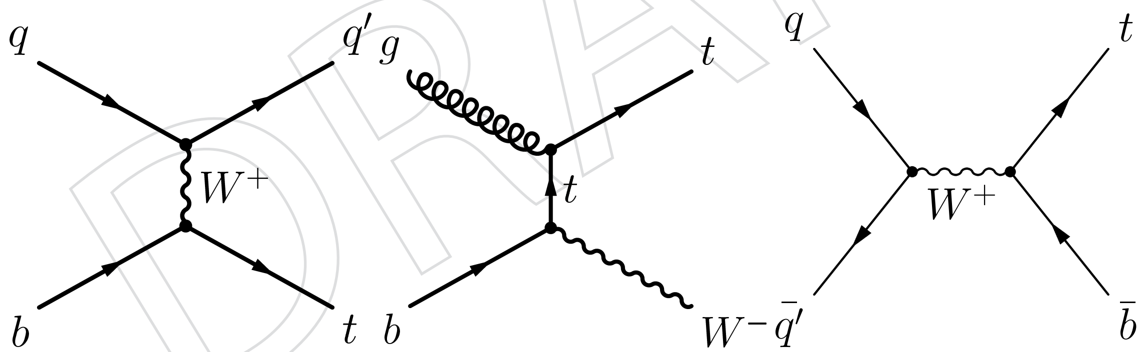

Figure 1: Feynman diagrams of single top production in the SM: *t*-channel (left) , tW-channel (middle) and *s*-channel (right).

As alluded earlier, most of the top-quark mass measurements till date have been obtained with $\mathrm{t\bar{t}}$ events. Single top process provides an independent statistical sample to measure the same quantity. This process occurs at a lower energy scale compared to $\mathrm{t\bar{t}}$. Further, it enriches the range of available measurements with systematics being partially uncorrelated from those considered for $\mathrm{t\bar{t}}$ events. The distinct production mechanism of the *t*-channel single top process dictates color connection only between the top quark and the proton, from which the initial b-quark is coming and not to the whole event as observed in $\mathrm{t\bar{t}}$ [5]. Such measurements therefore provide a useful check for any large unknown systematic effects arising due to the modeling of non-perturbative QCD processes in Monte Carlo (MC) simulations. Previous measurements of the top quark mass with single top events were performed by both CMS and ATLAS using full Run-1 data collected at a centre-of-mass energy $\sqrt{s}$ = 8 TeV [6, 7]; the respective results are:

$$m_t = 172.95 \pm 0.77\,(\text{stat.})\,^{+0.97}_{-0.93}\,(\text{syst.})\,\text{GeV}, \quad (2)$$

$$m_t = 172.2 \pm 0.7\,(\text{stat.})\, \pm 2.0\,(\text{syst.})\,\text{GeV} \quad (3)$$

In the analysis reported here, a measurement of the top quark mass is performed with t-channel single top events using 35.9 fb^{-1} data collected at $\sqrt{s}$ = 13 TeV by the CMS experiment during 2016. A striking feature of this channel is the presence of a light-flavor quark in the final state, recoiling against the top quark (antiquark) in the high pseudorapidity (η) region. The produced top quark (antiquark) almost exclusively decays to a bottom quark (antiquark) and a $W^{\pm}$ boson. This analysis is focused on the muon and electron final states arising from direct and cascade (via τ lepton) decays of the $W^{\pm}$ boson, originating from the top quark (antiquark) decay. The outgoing bottom quark (antiquark) hadronizes to a jet that can be identified ("b-tagged") using its characteristic signature inside the CMS detector. The four-momenta of the decay products of the top quark (antiquark) including the neutrino are either directly measured or estimated to calculate the invariant mass of the $\ell\nu$b system. An event selection based on the multivariate analysis (MVA) technique is designed to obtain a high-purity signal sample for the measurement. We measure the masses of top quark and antiquark separately by selecting events with positively and negatively charged leptons, respectively, in order to determine their mass difference as a test of the CPT invariance.

2 Data and MC Samples

2.1 Data samples

The analysis is based on the data recorded by CMS experiment, corresponding to a total integrated luminosity (L_{int}) of 35.9 fb^{-1}. Table 1 lists the different run periods used for each dataset. Only luminosity sections certified as good according to the so-called *Golden* JSON file
`Cert_271036-284044_13TeV_23Sep2016ReReco_Collisions16_JSON.txt`
are considered. Luminosities are quoted from the pixel cluster counting method and are known with an uncertainty of 2.5% [8].

Table 1: List of data samples over different run periods.

Run period	Run range	Dataset name	L_{int} (fb^{-1})
Run B	272007–275376	/SingleMuon(Electron)/Run2016B-03Feb2017_ver2-v2/MINIAOD	5.8
Run C	275657–276283	/SingleMuon(Electron)/Run2016C-03Feb2017-v1/MINIAOD	2.6
Run D	276315–276811	/SingleMuon(Electron)/Run2016D-03Feb2017-v1/MINIAOD	4.2
Run E	276831–277420	/SingleMuon(Electron)/Run2016E-03Feb2017-v1/MINIAOD	4.1
Run F	277772–278808	/SingleMuon(Electron)/Run2016F-03Feb2017-v1/MINIAOD	3.1
Run G	278820–280385	/SingleMuon(Electron)/Run2016G-03Feb2017-v1/MINIAOD	7.5
Run H	280919–284044	/SingleMuon(Electron)/Run2016H-03Feb2017_ver{2,3}-v1/MINIAOD	8.6
Total	272007–284044		35.9

2.2 Signal and Background MC samples

The t-channel single top quark and antiquark events are generated using the NLO generator POWHEG [9–11] within the four-flavor scheme and the parton distribution function (PDF) set NNPDF3.0 [12]. Several SM background processes are considered in the analysis. The $t\bar{t}$ process and production of single top quark and antiquark in association with a $W^{\mp}$ boson (tW) are generated with POWHEG. The latter is simulated within the five-flavor scheme. The value of the top quark mass used in these simulated samples is 172.5 GeV. The production of W or Z bosons in association with jets is generated using the MG5_aMC@NLO [13] event generator and the FxFx merging scheme [14]. For all these samples, PYTHIA 8 [15] is used to model the showering process. To validate the data-driven method for estimating the multijet background, QCD events are generated with PYTHIA 8. In Table 11, various simulation samples used in this analysis are listed. All generated events undergo a full simulation of the detector response according to an implementation of the CMS detector within GEANT 4 [16, 17]. Additional pp interactions (pileups) are included in the simulation with the same frequency of occurrence as observed in data.

Table 2: List of signal and background MC samples.

Process	$\sigma(\times BR)$[pb]	Dataset name	N_{events}
t-channel,top, inclusive decays	136.02 (NLO) [18]	ST_t-channel_top_4f_inclusiveDecays_13TeV-powhegV2-madspin-pythia8_TuneCUETP8M1	67240808
t-channel, anti-top, inclusive decays	80.95 (NLO) [18]	ST_t-channel_antitop_4f_inclusiveDecays_13TeV-powhegV2-madspin-pythia8_TuneCUETP8M1	38811017
s-channel, top+anti-top, leptonic decays	10.32($\times$ 0.324) (NNLL) [18]	ST_s-channel_4f_leptonDecays_13TeV-amcatnlo-pythia8_TuneCUETP8M1	1000000
tW-channel, top, inclusive decays	35.6 (NNLL) [18]	ST_tW_top_5f_inclusiveDecays_13TeV-powheg-pythia8_TuneCUETP8M2T4	992024
tW-channel, anti-top, inclusive decays	35.6 (NNLL) [18]	ST_tW_antitop_5f_inclusiveDecays_13TeV-powheg-pythia8_TuneCUETP8M1	998276
$t\bar{t}$, inclusive decays	831.76 (NNLO+NNLL) [18]	TT_TuneCUETP8M2T4_13TeV-powheg-pythia8	77229341
W($\rightarrow \ell\nu$)+0 jet	50132 (NNLO)	WToLNu_0J_13TeV-amcatnloFXFX-pythia8	49141548
W($\rightarrow \ell\nu$)+1 jet	8426 (NNLO)	WToLNu_1J_13TeV-amcatnloFXFX-pythia8	92024405
W($\rightarrow \ell\nu$)+2 jets	3173 (NNLO)	WToLNu_2J_13TeV-amcatnloFXFX-pythia8	102093848
$Z/\gamma^*(\rightarrow \ell^+\ell^-)$+jets ($M_{\ell\ell} > 50$ GeV)	5765.4 (NNLO)	DYJetsToLL_M-50_TuneCUETP8M1_13TeV-amcatnloFXFX-pythia8	28968252
WW$\rightarrow 1\ell 1\nu 2$q	45.85 (NLO)	WWTo1L1Nu2Q_13TeV_amcatnloFXFX_madspin_pythia8	5176114
WW$\rightarrow 2\ell 2\nu$	12.178 (NLO)	WWTo2L2Nu_13TeV-powheg	1999000
WZ$\rightarrow 1\ell 1\nu 2$q	10.71 (NLO)	WZTo1L1Nu2Q_13TeV_amcatnloFXFX_madspin_pythia8	24221923
WZ$\rightarrow 2\ell 2$q	5.595 (NLO)	WZTo2L2Q_13TeV_amcatnloFXFX_madspin_pythia8	26517272
ZZ$\rightarrow 2\ell 2$q	3.22 (NLO)	ZZTo2L2Q_13TeV_amcatnloFXFX_madspin_pythia8	15345572
μ-enriched QCD	302672.16 (LO)	QCD_Pt-20toInf_MuEnrichedPt15_TuneCUETP8M1_13TeV_pythia8	22094081
EM-enriched QCD	5352960 (LO)	QCD_Pt-20to30_EMEnriched_TuneCUETP8M1_13TeV_pythia8	9218954
	9928000 (LO)	QCD_Pt-30to50_EMEnriched_TuneCUETP8M1_13TeV_pythia8	6768384
	2890800 (LO)	QCD_Pt-50to80_EMEnriched_TuneCUETP8M1_13TeV_pythia8	23474171
	350000 (LO)	QCD_Pt-80to120_EMEnriched_TuneCUETP8M1_13TeV_pythia8	41853504
	62964 (LO)	QCD_Pt-120to170_EMEnriched_TuneCUETP8M1_13TeV_pythia8	41954035
	18810 (LO)	QCD_Pt-170to300_EMEnriched_TuneCUETP8M1_13TeV_pythia8	11540163
	1350 (LO)	QCD_Pt-300toInf_EMEnriched_TuneCUETP8M1_13TeV_pythia8	7373633

3 Object Selection

Various objects used in the analysis are reconstructed with information from all CMS subdetectors based on the particle-flow (PF) algorithm [19].

3.1 Trigger

Events are required to pass the high-level trigger (HLT) criteria for each of the leptonic final states.

- For events containing a muon in the final state, a logical `OR` of the trigger decisions `HLT_IsoMu24` and `HLT_IsoTkMu24` needs to be satisfied, which demands the presence of at least one isolated "global muon" (reconstructed with information from the inner tracker as well as the muon chambers) `OR` "tracker muon" (reconstructed with information from the inner tracker and minimal information from the muon chambers) candidate with transverse momentum, $p_T > 24$ GeV.
- For events with an electron in the final state, `HLT_Ele32_eta2p1_WPTight_Gsf` needs to be satisfied, which demands the presence of at least one electron with p_T > 32 GeV and $|\eta| < 2.1$ passing the tight identification criteria.

3.2 Primary Vertex

Primary vertices are reconstructed by means of the standard deterministic-annealing clustering algorithm [20]. The first vertex in the collection (the one with largest sum of p_T^2 for the associated clustered objects [21]) is required to be within a cylinder of radius 2 cm around the beam axis and its z-coordinate must satisfy $|z| < 24$ cm. In addition, the reconstruction algorithm must not mark the vertex as `fake` and must assign it at least four degrees of freedom, which roughly corresponds to the requirement of at least four tracks being associated with the vertex. The vertices that satisfy the above requirements are exploited to mitigate the deleterious effects of pileup based on the charged-hadron subtraction scheme [22]. In this scheme, if a PF candidate is identified as a charged hadron and is associated to any but the first of these vertices, the candidate is removed from the event.

3.3 Tight Muons

Muons are reconstructed as `global muons`. Events with exactly one muon with $p_T > 26\,\mathrm{GeV}$ and within $|\eta| < 2.4$ are selected. These selected high-p_T muon objects are required to pass additional quality requirements to be identified as tight muons" [23]. Further, the muon must be well isolated in terms of the PF-based "$\Delta\beta$"-corrected relative isolation:

$$I_{rel} = \frac{I^{ch} + \max.[(I^{\gamma} + I^{nh} - 0.5 \times I^{PU}), 0]}{p_T^{\mu}} \tag{4}$$

where I^{ch}, I^{γ} and I^{nh} are the sum of the transverse energies of charged hadrons, photons and neutral hadrons, respectively, in a cone size of $\Delta R = \sqrt{(\Delta\eta)^2 + (\Delta\phi)^2} = 0.4$ around the muon direction. $I^{PU}$is the $\sum p_T^{PU}$ of charged hadrons associated to the vertices other than the primary vertex. It is used to estimate the contribution of neutral particles from pileup vertices, where the factor 0.5 takes into account the neutral-to-charged particle ratio. For the tight muon, our selection requires $I_{rel} < 0.06$.

3.4 Tight Electrons

Similar to the case of muons,"tight" electrons are required for the events with electron final state. Such an electron must pass the tight working point of the cut-based identification criteria [24] and must not be identified as originating from a photon conversion. The "tight" electron must have $p_T > 35\,\mathrm{GeV}$ and $|\eta| < 2.1$, excluding the transition region between the barrel and endcap of the electromagnetic calorimeter, given by $1.4442 < |\eta_{sc}| < 1.5660$, where η_{sc} is the pseudorapidity of the supercluster associated to the electron track. Additional requirements on the transverse and longitudinal impact parameters (d_{xy} and d_z) are applied separately for the barrel and endcap regions. In the barrel region ($|\eta| \leq 1.479$), eletrons are required to pass $d_{xy} < 0.05$ cm and $d_z < 0.1$ cm criteria, whereas in the endcap region ($|\eta| > 1.479$), they need to satisfy $d_{xy} < 0.1$ cm and $d_z < 0.2$ cm.

3.5 Loose Muons

Events with additional muons are vetoed. The requirements for having one or more additional muon in the event are loosened. Events having another muon with $p_T > 10\,\mathrm{GeV}$ within $|\eta| < 2.4$ that satisfies the "global muon" `OR` "tracker muon" criteria (muons reconstructed in the inner tracker having at least one segment in the muon chambers) and $I_{rel} < 0.2$, are rejected.

3.6 Veto Electrons

Events with one or more electrons along with the tight lepton, described in Sections 3.3 and 3.4, are vetoed. Any event which contains additional electron(s) with $E_T > 15$ GeV within $|\eta| < 2.5$ passing the cut-based "veto" identification criteria is rejected.

3.7 Jets

Jets are reconstructed using the anti-k_T algorithm [25] with a cone size of 0.4, taking PF candidates as inputs after rejecting charged hadrons associated to pileup vertices (slimmedJets). We require at least two jets having $p_T > 40$ GeV and $|\eta| < 4.7$. To reduce the contamination of fake jets from pileup vertices or detector noise, a set of $|\eta|$-dependent "loose" identification criteria [26] are applied. Jets are also required to have $\Delta R > 0.4$ relative to the selected tight lepton described earlier.
Once the jets are reconstructed, a number of corrections [27] are applied to their measured energy. Sequentially, we apply `L1Fastjet`, `L2Relative` and `L3Absolute` corrections from payload `Summer16_23Sep2016V4` to both data and simulation, in order to reduce contribution from pileup as well as to account for the nonlinear calorimetric response and detector mismodeling depending on p_T and $|\eta|$ of the jet. The `L2L3Residual` corrections are applied to data only, while the jet energy in simulated samples is smeared to account for the p_T difference observed between the reconstructed and associated generated jet in data to those in the simulations [28] corresponding to the tag `Summer16_25ns_v1`.

3.8 B-tagging

As the lifetime of a b-flavored hadron is large, it travels certain distance before decaying. Within CMS various techniques have been explored to identify jets that originate from bottom quarks or antiquarks using the secondary vertex and lifetime information. For this study, a combined MVA algorithm ("cMVAv2") [29] has been used which collects track-based lifetime information together with secondary vertices inside the jet to provide an optimal MVA discriminator for b-jet identification. We apply a "tight" threshold on the discriminator value (> 0.9432) that corresponds to an average b-tagging efficiency of $\approx 55\%$ with a light-flavor misidentification probability of 0.1%.

3.9 Missing Transverse Momentum

The missing transverse momentum vector $\overrightarrow{\not{p}_{\mathrm{T}}}$ is defined as the projection of the negative vector sum of the momenta of all reconstructed PF objects in an event onto the plane perpendicular to the beam axis:

$$\overrightarrow{\not{p}_{\mathrm{T}}} = -\sum_i \overrightarrow{p_{\mathrm{T},i}} \quad (5)$$

where i refers to the i-th PF candidate. Its magnitude is referred to as $\not{p}_{\mathrm{T}}$. To account for possible misreconstructed high-p_T muons in the 2016 data, the `slimmedMETsMuEGClean` collection instead of the default `slimmedMETs` is used for the missing transverse momentum calculation [30].

3.10 Transverse W-boson Mass

The transverse W-boson mass is defined as:

$$m_{\mathrm{T}}^{\mathrm{W}} = \sqrt{(p_{\mathrm{T},\ell} + \not{p}_{\mathrm{T}})^2 - (p_{x,\ell} + \not{p}_x)^2 - (p_{y,\ell} + \not{p}_y)^2} \quad (6)$$

where, $p_{x,\ell}$ and $p_{y,\ell}$ are the x and y-component of the tight lepton momentum and $\not{p}_x$ and $\not{p}_y$ are the same components of $\overrightarrow{\not{p}_T}$. As m_T^W is very sensitive to the processes with prompt leptons from the leptonically decaying W boson, a cut of $m_T^W > 50$ GeV is applied to suppress contributions from processes with nonprompt muons in the case of μ+jets events.

3.11 MC Correction Factors

A number of correction factors are applied to MC simulation to match with data. They are described below.

- **Pileup Reweighting**: The pileup profile used in the MC simulation does not agree exactly with that in data where the latter is derived from the (effective) total cross section of inelastic pp scattering and the measured instantaneous luminosity. To correct for this difference, MC events are reweighted based on the *true* number of pileup interactions, as suggested by the standard prescription [31], assuming a minimum-bias cross section of 69.2 mb for the pileup reweighting [32]. An additional systematic uncertainty is introduced by varying this cross section by $\pm 4.6\%$.
- **Lepton Efficiencies**: The correction of the muon efficiencies encompasses separate scale factors for the muon identification and tracker efficiencies. The correction factors are provided by the Muon POG [33], which are derived with tag-and-probe methods [34] at the J/ψ and Z boson resonances. As the official muon isolation and trigger scale factors are not suitable for this analysis owing to the tight isolation criterion on $I_{rel} < 0.06$, privately produced correction factors [35] are applied instead.
  Simulated electron efficiencies for the reconstruction as well as cut-based identification are also corrected [36]. The correction factors are provided by the EGamma POG that have been determined on large $Z \rightarrow e^+e^-$ samples with the tag-and-probe procedure [37]. The correction of the electron trigger efficiency is applied too; since the EGamma POG does not provide this efficiency, the privately produced correction scale factors [35] are used.
  The determination of these lepton scale factors depends on the available amount of data and simulated events. Hence, the statistical uncertainty of each scale factor is used as an additional source of systematic uncertainty.
- **B-tagging Efficiency**: In order to account for differences in b-tagging efficiency of the cMVAv2 algorithm between data and simulations, MC simulated events are reweighted following the method described in Ref. [38]. The probablity of having n b-tagged jets and m not-b-tagged (untagged) jets in simulation and data are given by:

$$P(\mathrm{MC}) = \prod_{i=\mathrm{tagged}}^{n} \epsilon_i \prod_{j=\mathrm{untagged}}^{m} (1-\epsilon_j), \tag{7}$$

$$P(\mathrm{Data}) = \prod_{i=\mathrm{tagged}}^{n} \mathrm{SF}_i\epsilon_i \prod_{j=\mathrm{untagged}}^{m} (1-\mathrm{SF}_j\epsilon_j), \tag{8}$$

  where ϵ_i is the b-tagging efficiency in simulation and SF_i are the scale factors for the cMVAv2 algorithm that are provided by the BTV POG [39]. Both the scale factors and b-tagging efficiencies depend on the jet flavor, p_T and η. The event weight is then given by

$$w = \frac{P(\mathrm{Data})}{P(\mathrm{MC})} \tag{9}$$

4 Event Categorization: Signal and Control Regions

The *t*-channel single top production mode has one light quark recoiling against the virtual W boson and one b-quark arising from the top quark decay. There is a second b-quark in the final state due to the initial gluon splitting at NLO. The p_T-spectrum of the latter b-quark is softer compared to the one coming from the top quark. It also has large $|\eta|$ as opposed to the b-quark originating from top that goes more centrally within the detector. As a result, the jet due to the second b-quark in the final state is often either rejected by the jet p_T-threshold (> 40 GeV) applied during selection or not identified as a b-tagged jet due to limited tracker acceptance ($|\eta| < 2.4$). Hence, the region with two jets, with one of them being b-tagged, has the largest fraction of signal events.
Depending on the number of jets and the number of b-tagged jets, we define several event categories in addition to the signal-enriched region. These are used to validate the normalization and modeling of dominant background processes. A generic nomenclature "nJmT" is attributed to the events having "n" jets and "m" b-tagged jets. In addition to the signal-enriched 2J1T region; 2J0T, 3J1T and 3J2T regions have been extensively studied as various control regions.

4.1 2J1T Region

This is the region with highest signal fraction. The b-tagged jet is identified to originate from the b-quark due to the top decay, while the untagged jet is identified to recoil against the top quark. The sideband defined by $I_{rel} > 0.2$ is used to estimate the QCD contribution in 2J1T as explained in Section 7.2. An MVA technique is used in this region to reduce the electroweak and top backgrounds as described in Section 8. Kinematic plots of the final state objects in the 2J1T region before applying m_T^W cut are shown in Figures 2 to 5.

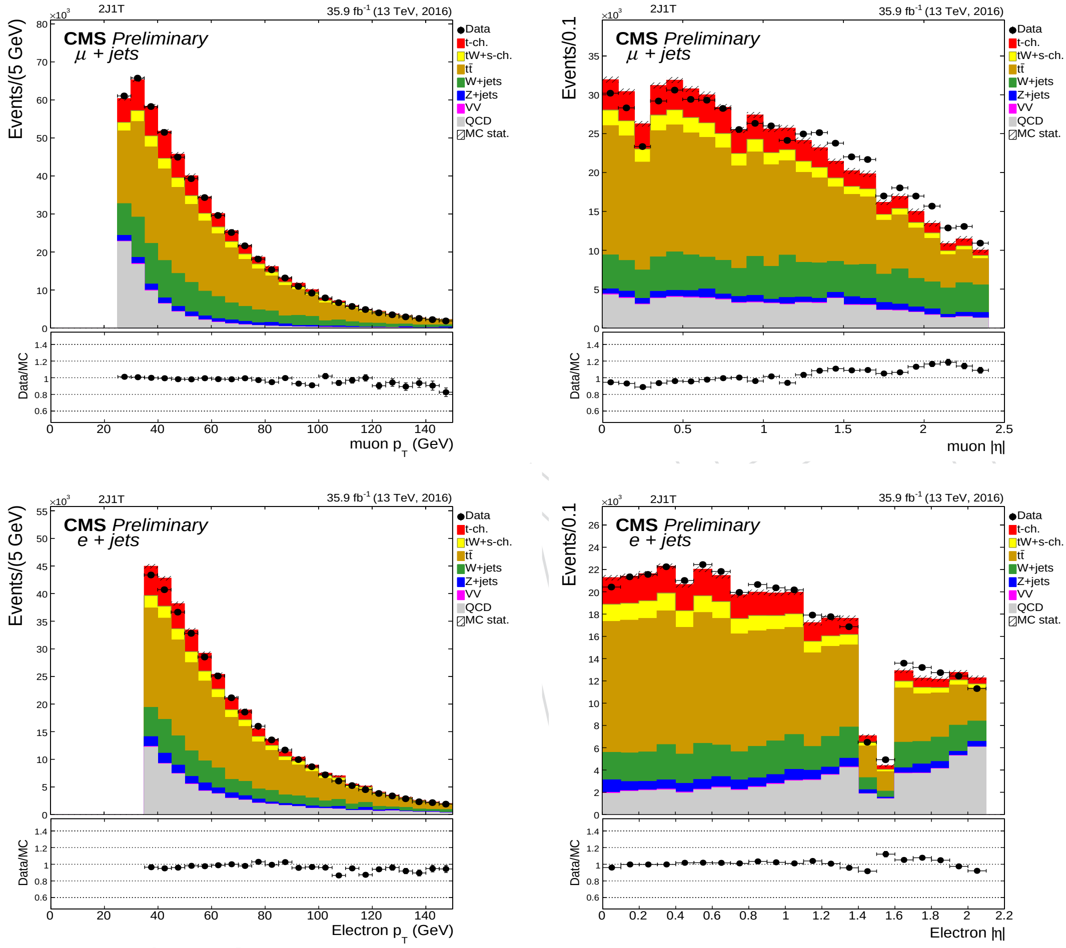

Figure 2: Data-MC comparison of p_T (left) and $|\eta|$ (right) corresponding to muon (top) and electron (bottom) final states in 2J1T.

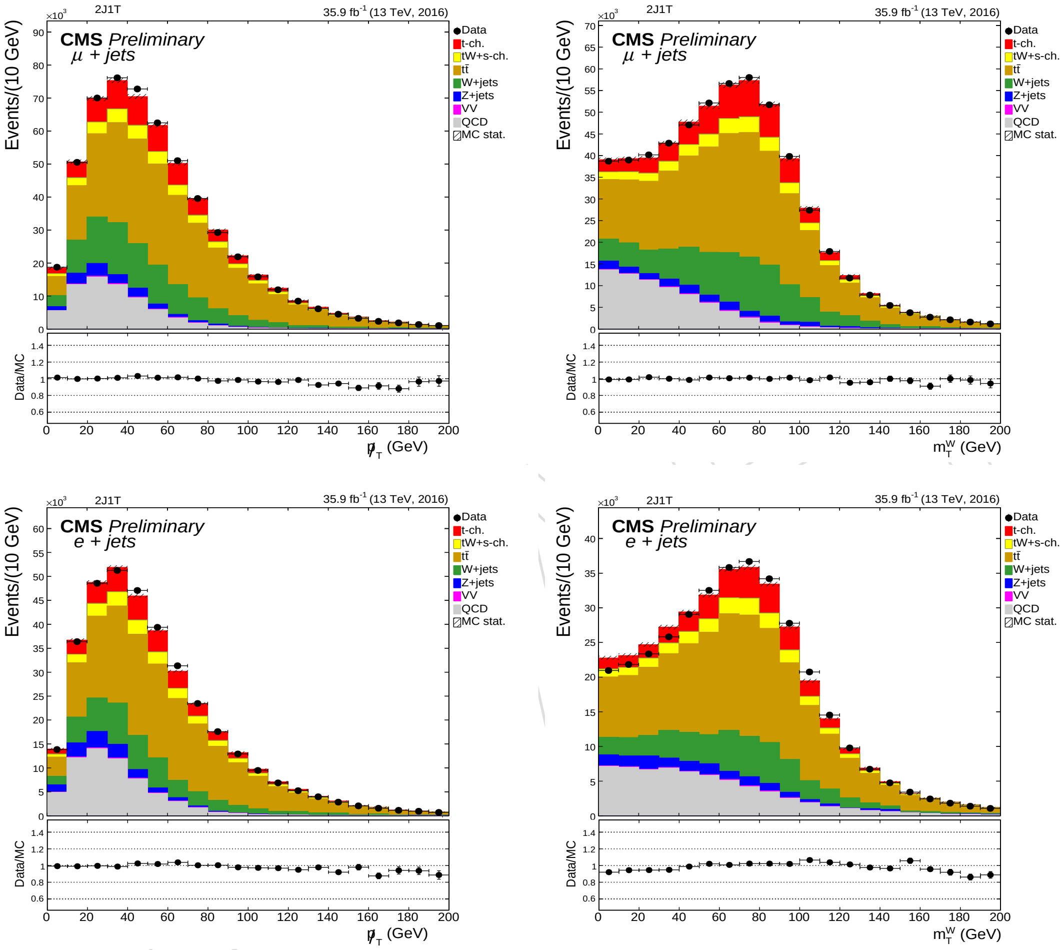

Figure 3: Data-MC comparison of $\not{p}_T$ (left) and m_T^W (right) corresponding to muon (top) and electron (bottom) final states in 2J1T.

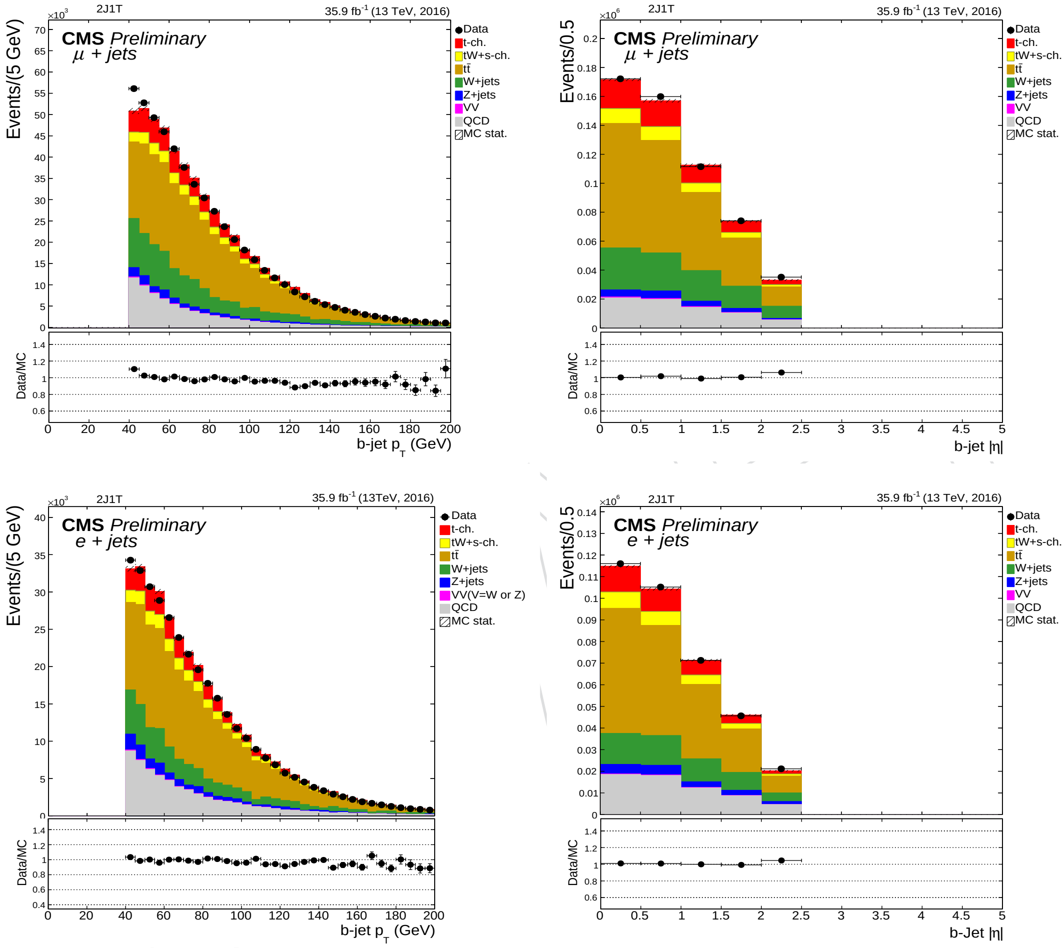

Figure 4: Data-MC comparison of b-jet p_T (left) and $|\eta|$ (right) corresponding to muon (top) and electron (bottom) final states in 2J1T.

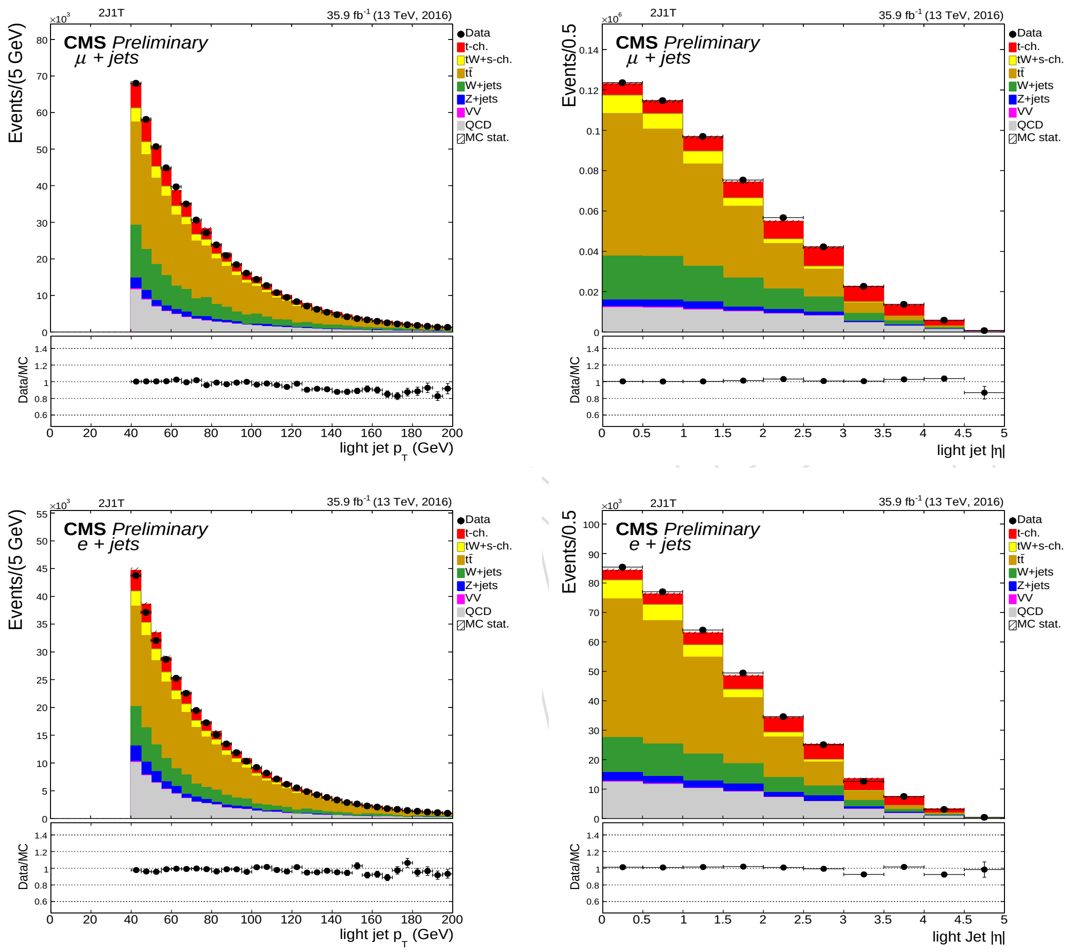

Figure 5: Data-MC comparison of light-flavor jet p_T (left) and $|\eta|$ (right) corresponding to muon (top) and electron (bottom) final states in 2J1T.

4.2 2J0T Region

This region is selected by requiring none of the two jets pass the tight b-tagging criteria. However, one of the jets is designated as the b-jet from top quark decay using the definitions in Section 6. The 2J0T region is dominated by W+light-flavor jets and QCD background. High QCD statistics in this region, which is adjacent but orthogonal to the signal region, serves well to validate the technique of QCD estimation to be applied to the signal region. The basic kinematic plots in the 2J0T region before applying cut to m_T^W is shown in Figures 6 to 9.

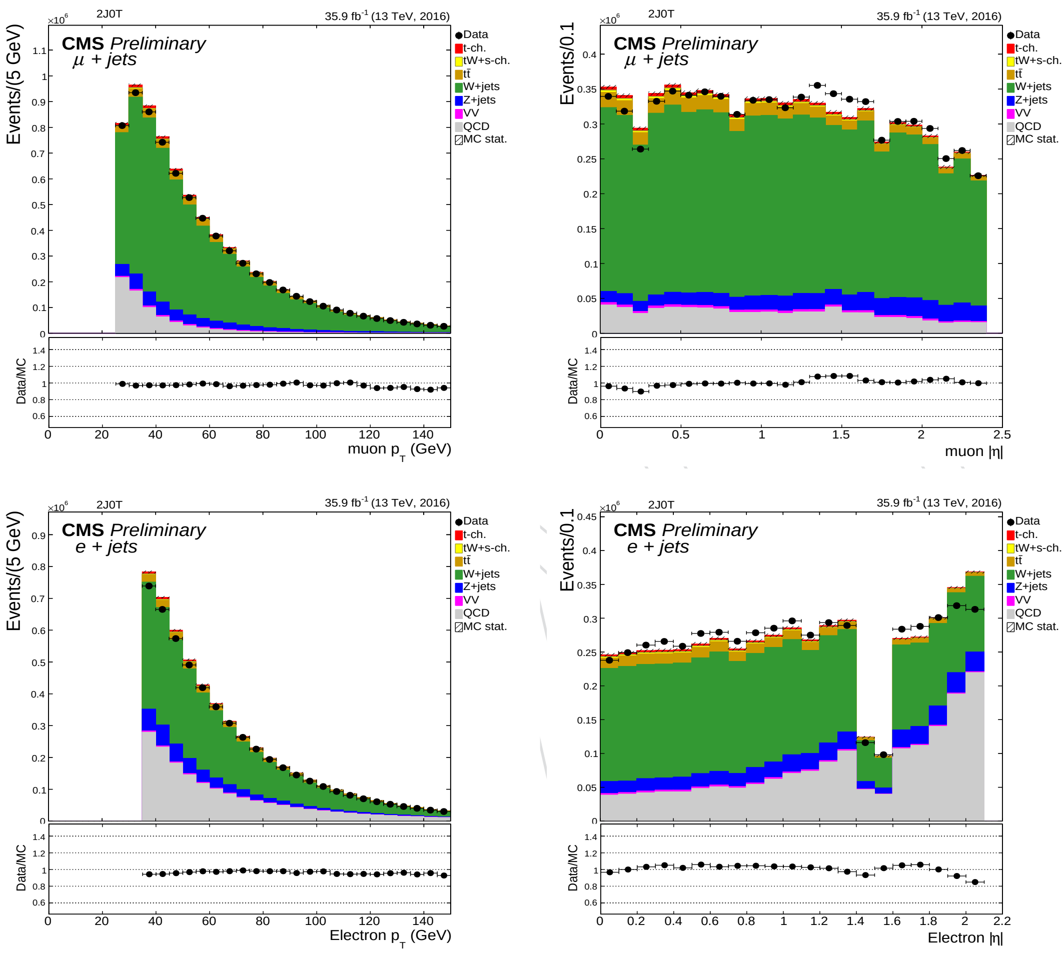

Figure 6: Data-MC comparison of lepton p_T (left) and $|\eta|$ (right) corresponding to muon (top) and electron (bottom) final states in 2J0T.

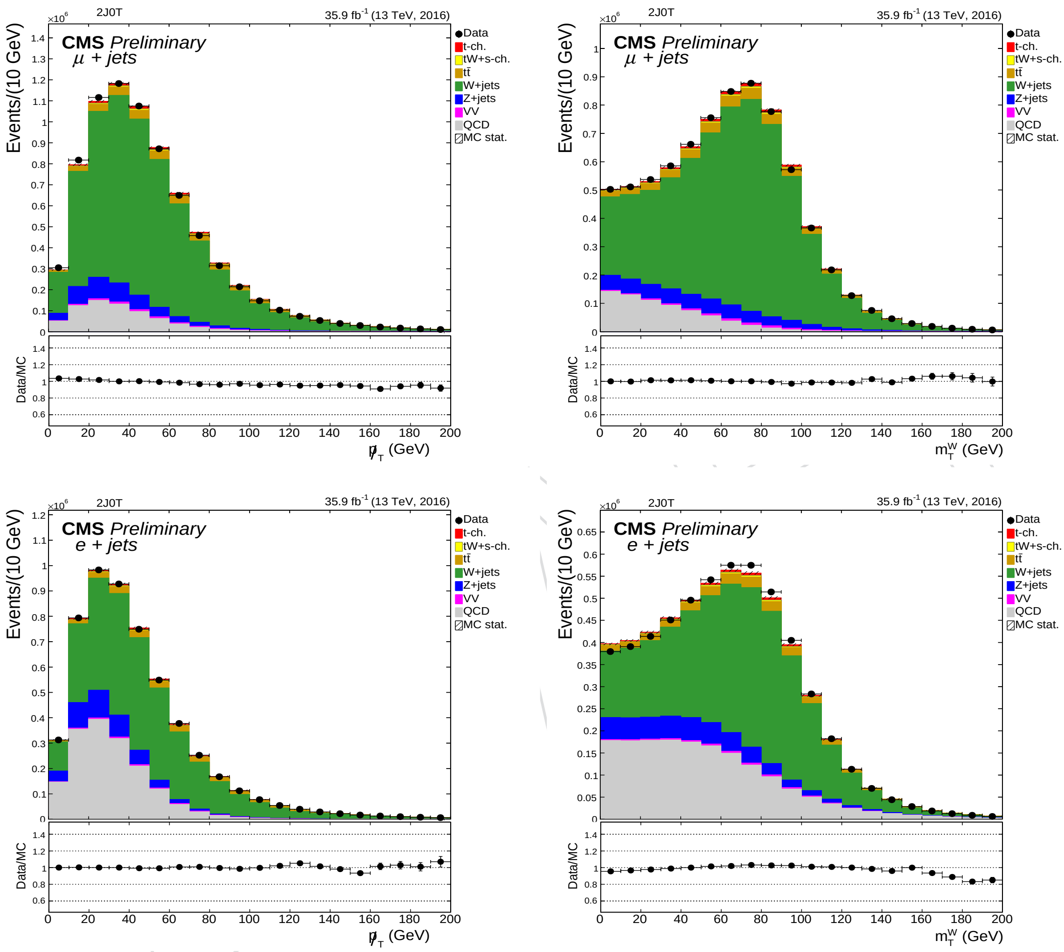

Figure 7: Data-MC comparison of $\not{p}_T$ (left) and m_T^W (right) corresponding to muon (top) and electron (bottom) final states in 2J0T.

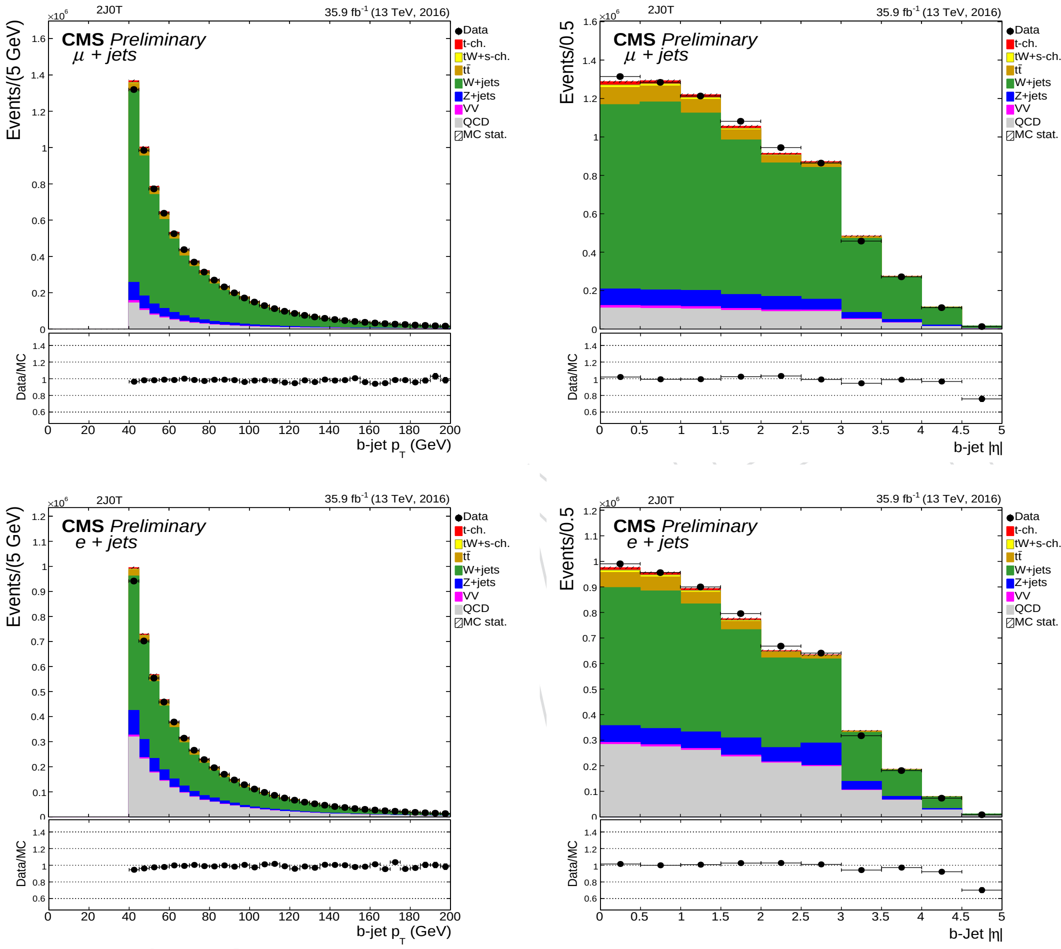

Figure 8: Data-MC comparison of b-jet p_T (left) and $|\eta|$ (right) corresponding to muon (top) and electron (bottom) final states in 2J0T.

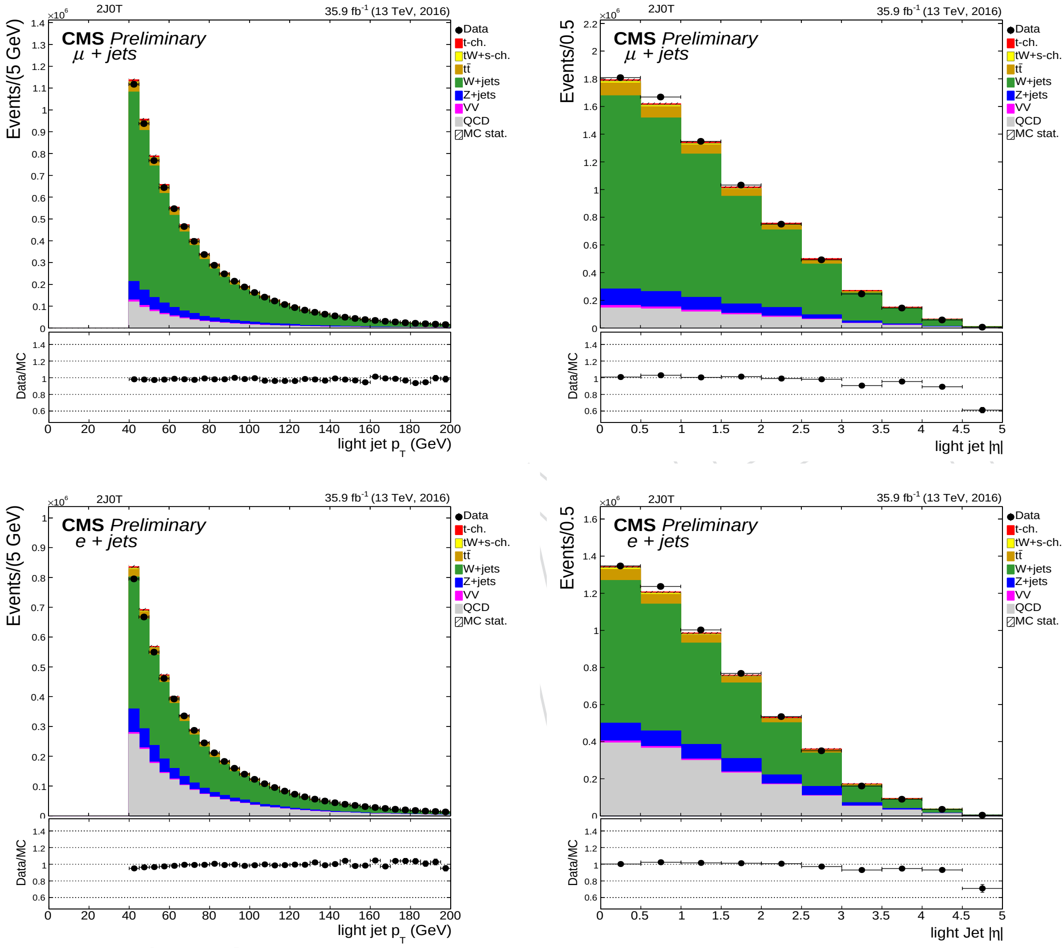

Figure 9: Data-MC comparison of light-flavor jet p_T (left) and $|\eta|$ (right) corresponding to muon (top) and electron (bottom) final states in 2J0T.

4.3 3J1T Region

This region is selected by requiring three jets passing the jet selection criteria, one of them being b-tagged. The 3J1T region is mostly dominated by $t\bar{t}$ background and has similar heavy flavor content as the signal region (2J1T). Therefore, this region is used to validate the modeling and normalization of events having a W boson produced in association with heavy flavor quarks. The basic kinematic plots before applying the m_T^W cut are shown in Figures 11 to 13.

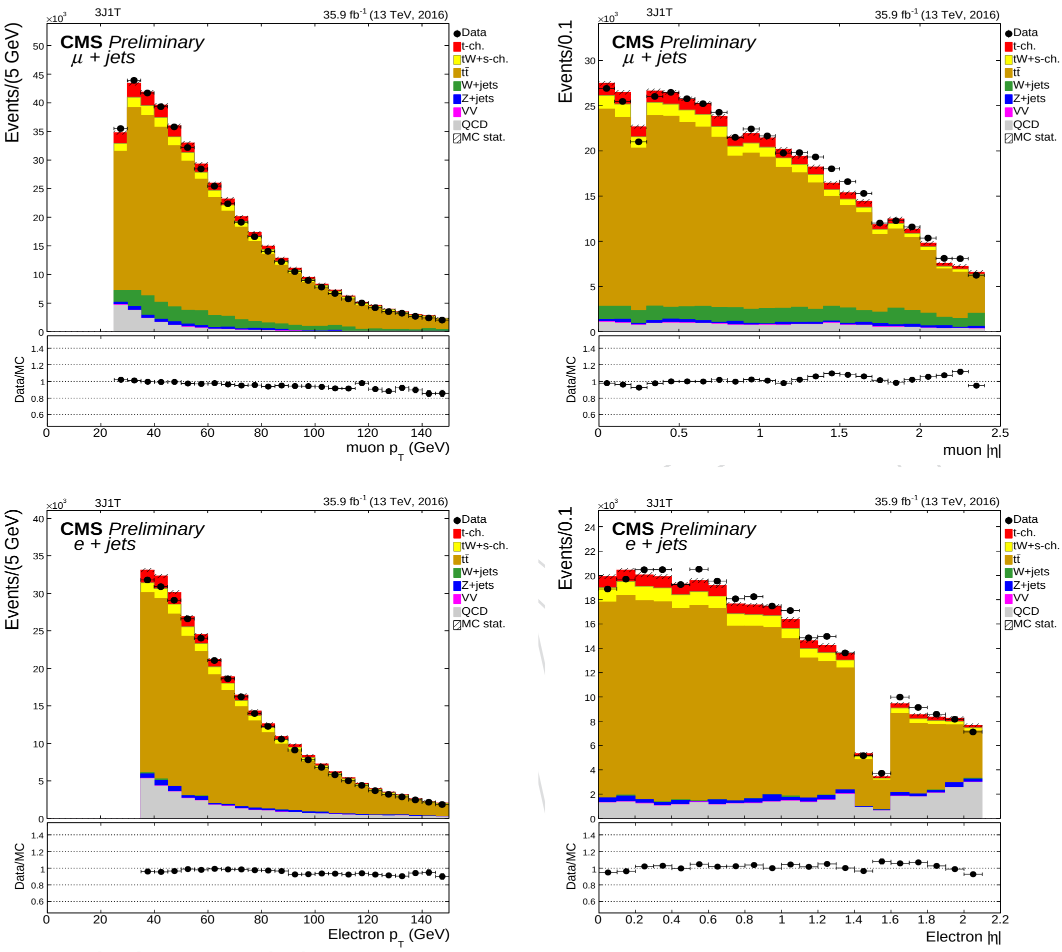

Figure 10: Data-MC comparison of lepton p_T (left) and $|\eta|$ (right) corresponding to muon (top) and electron (bottom) final states in 3J1T.

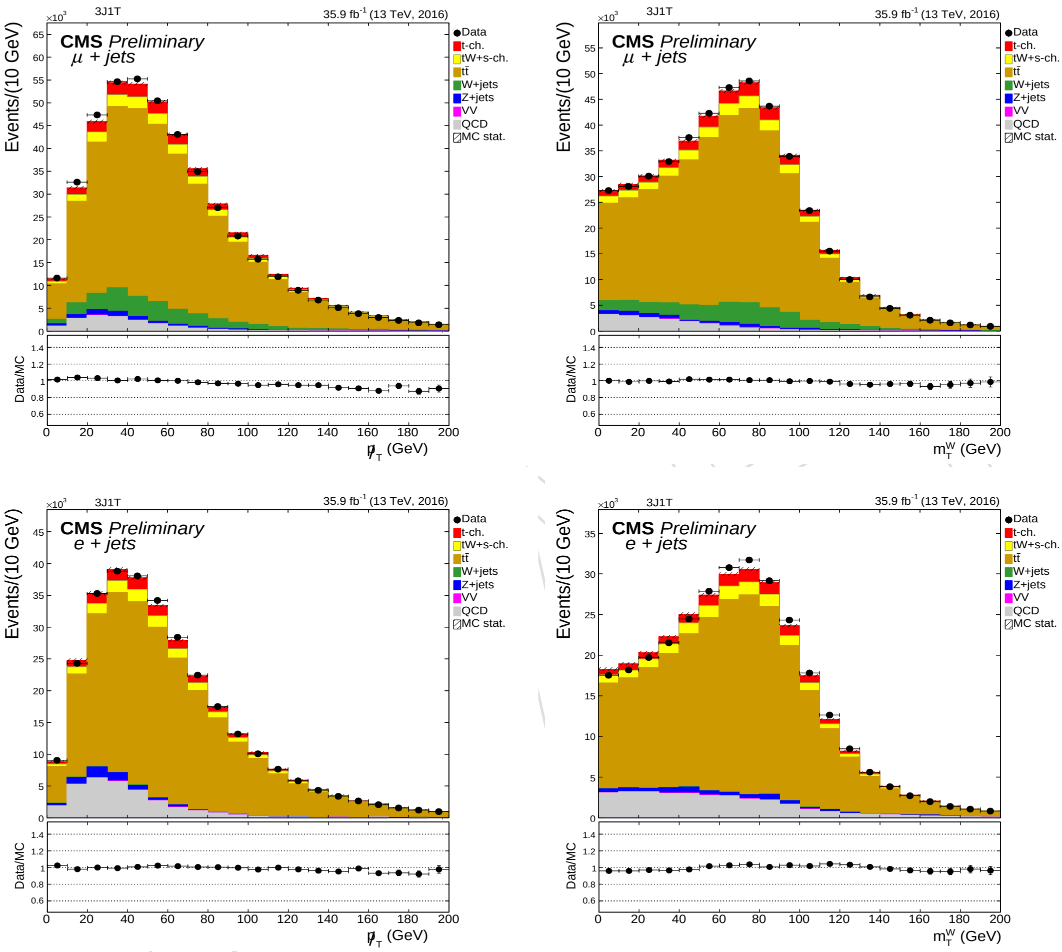

Figure 11: Data-MC comparison of $\not{p}_T$ (left) and m_T^W (right) corresponding to muon (top) and electron (bottom) final states in 3J1T.

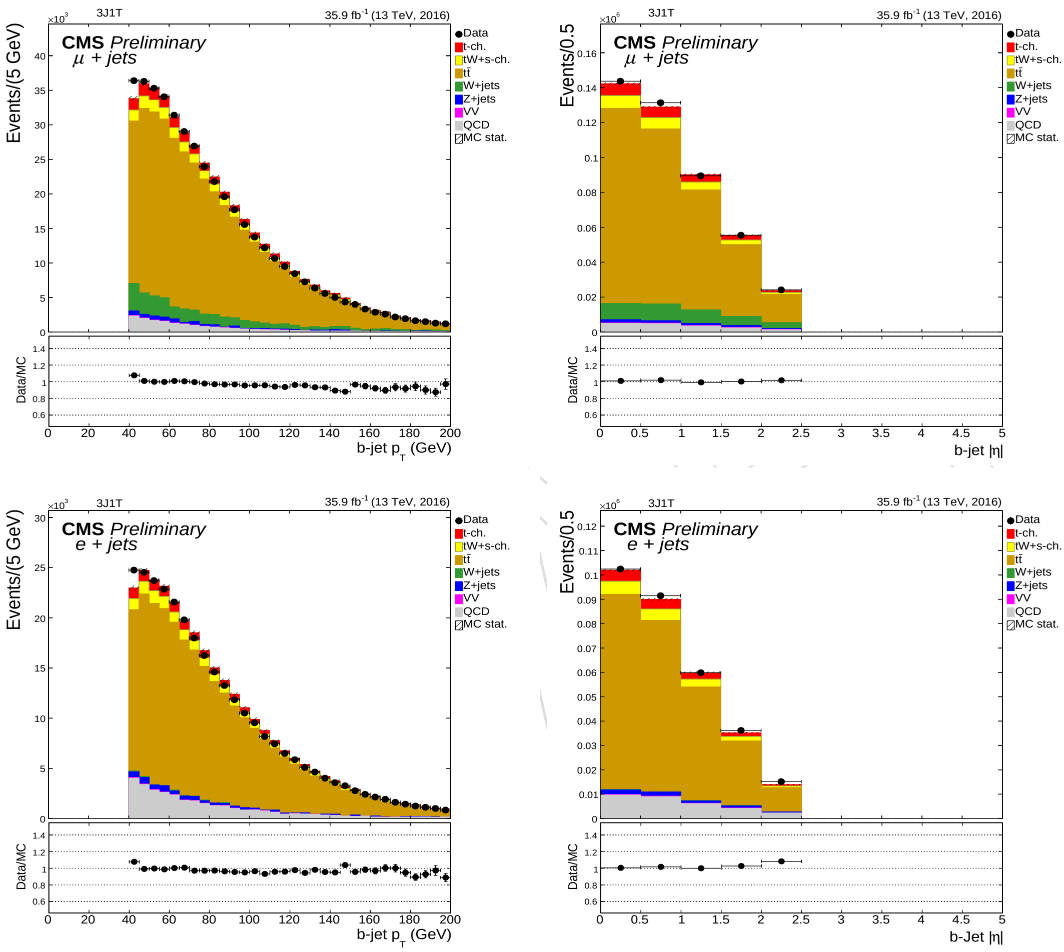

Figure 12: Data-MC comparison of b-jet p_T (left) and $|\eta|$ (right) corresponding to muon (top) and electron (bottom) final states in 3J1T.

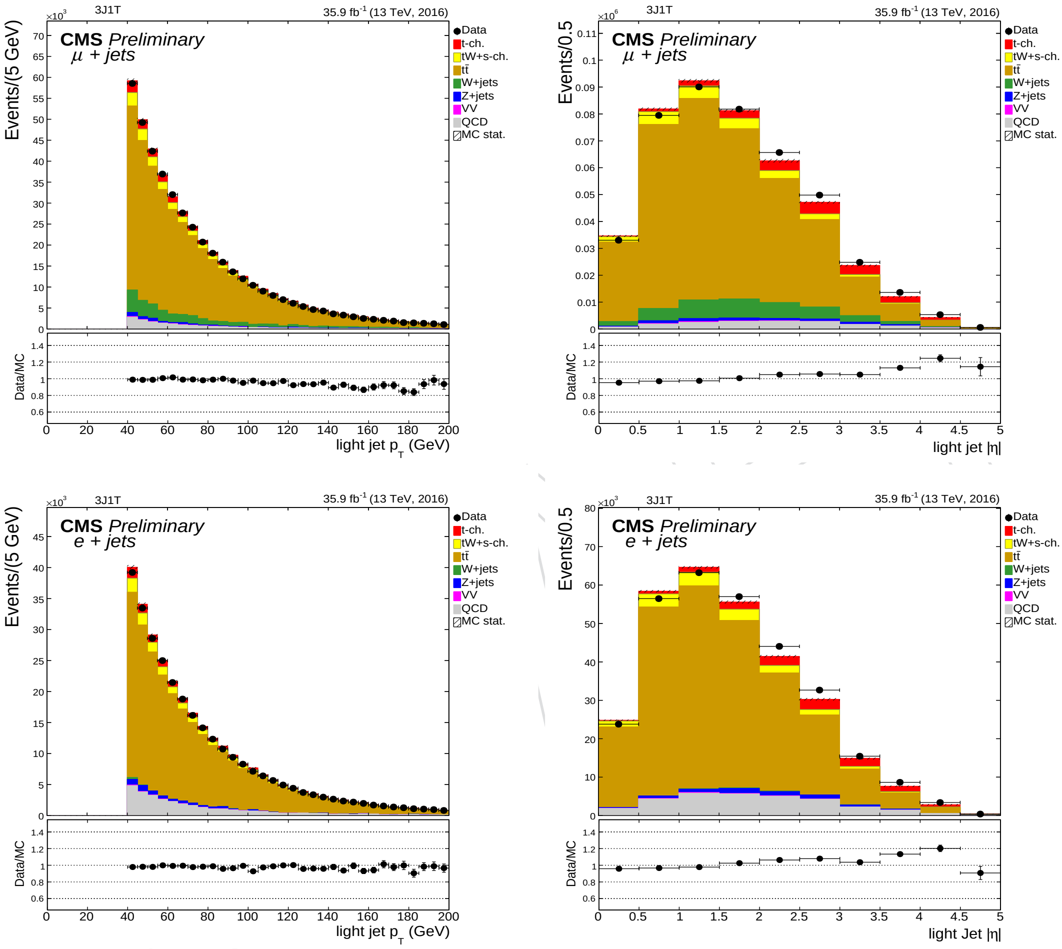

Figure 13: Data-MC comparison of light-flavor jet p_T (left) and $|\eta|$ (right) corresponding to muon (top) and electron (bottom) final states in 3J1T.

4.4 3J2T region

This region is selected by requiring three jets passing the jet selection criteria, two of them being b-tagged. The untagged jet is considered as the light-flavor jet. The jet due to the b-quark from top quark decay is identified as described in Section 6. This region is completely dominated by $t\bar{t}$ background. Therefore, 3J2T is used to validate the modeling and normalization of $t\bar{t}$ background. The basic kinematic plots in the 3J2T region before applying the m_T^W cut are shown in Figures 14 to 17.

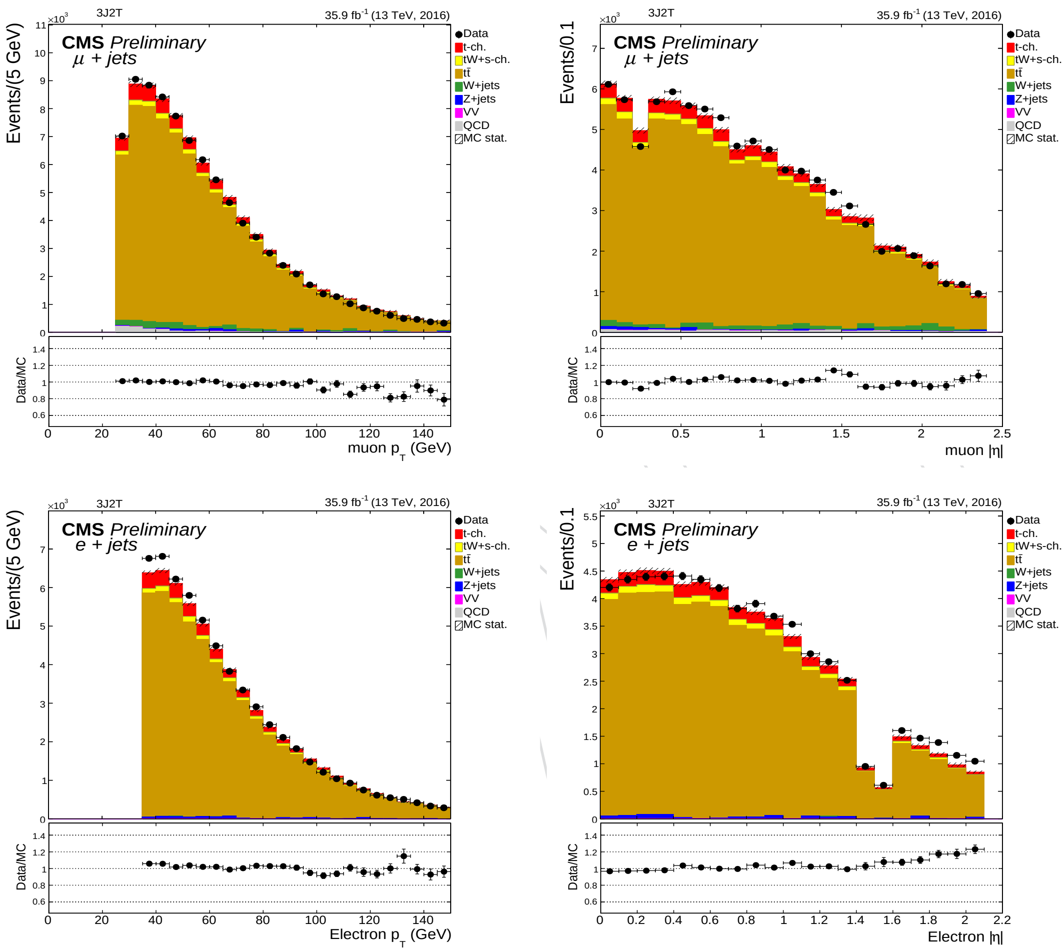

Figure 14: Data-MC comparison of lepton p_T (left) and $|\eta|$ (right) corresponding to muon (top) and electron (bottom) final states in 3J2T.

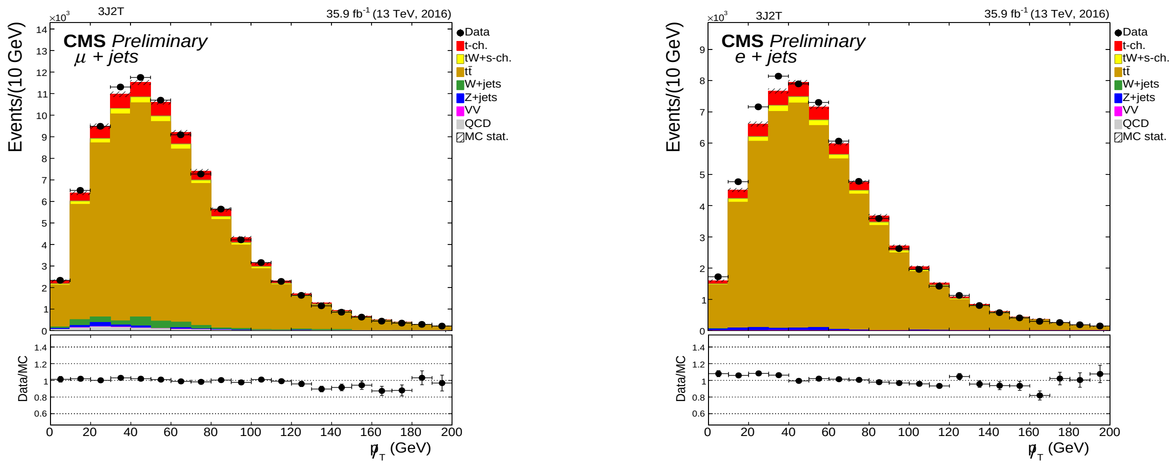

Figure 15: Data-MC comparison of $\not{p}_T$ corresponding to muon (top) and electron (bottom) final states in 3J2T.

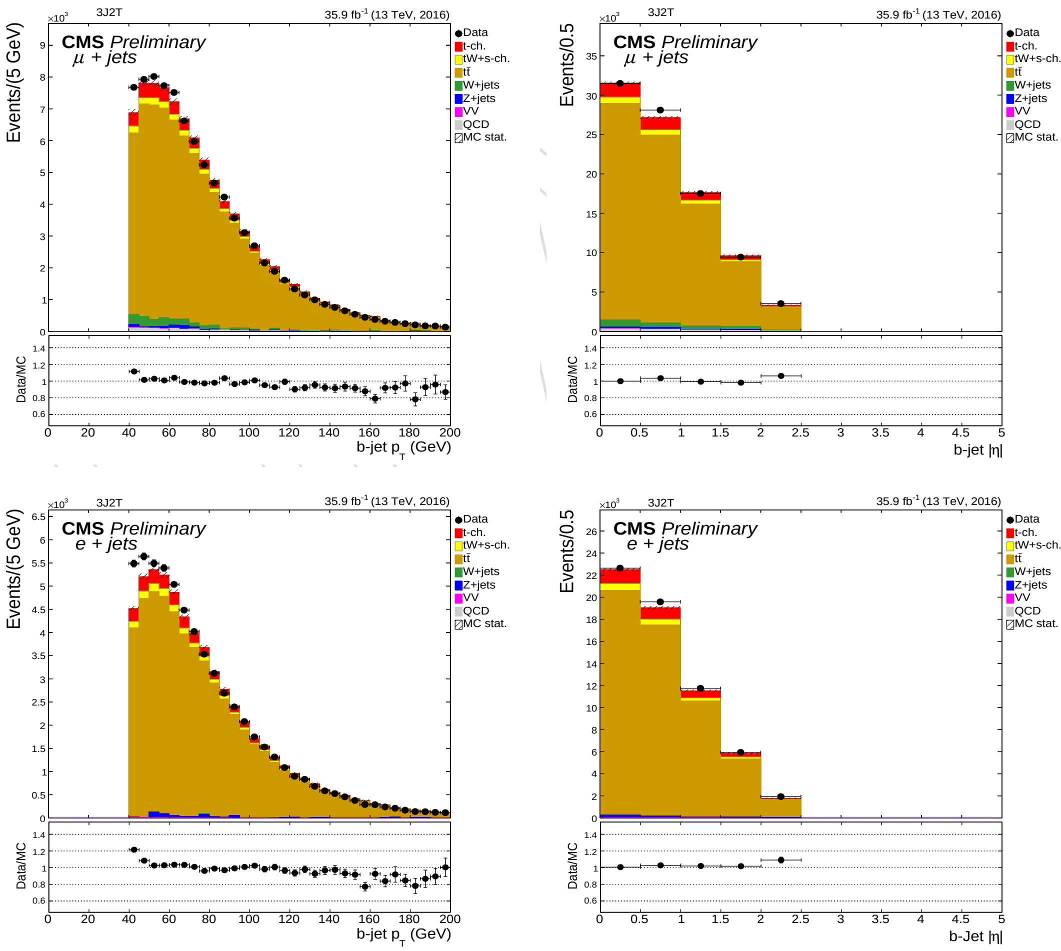

Figure 16: Data-MC comparison of b-jet p_T (left) and $|\eta|$ (right) in corresponding to muon (top) and electron (bottom) final states 3J2T.

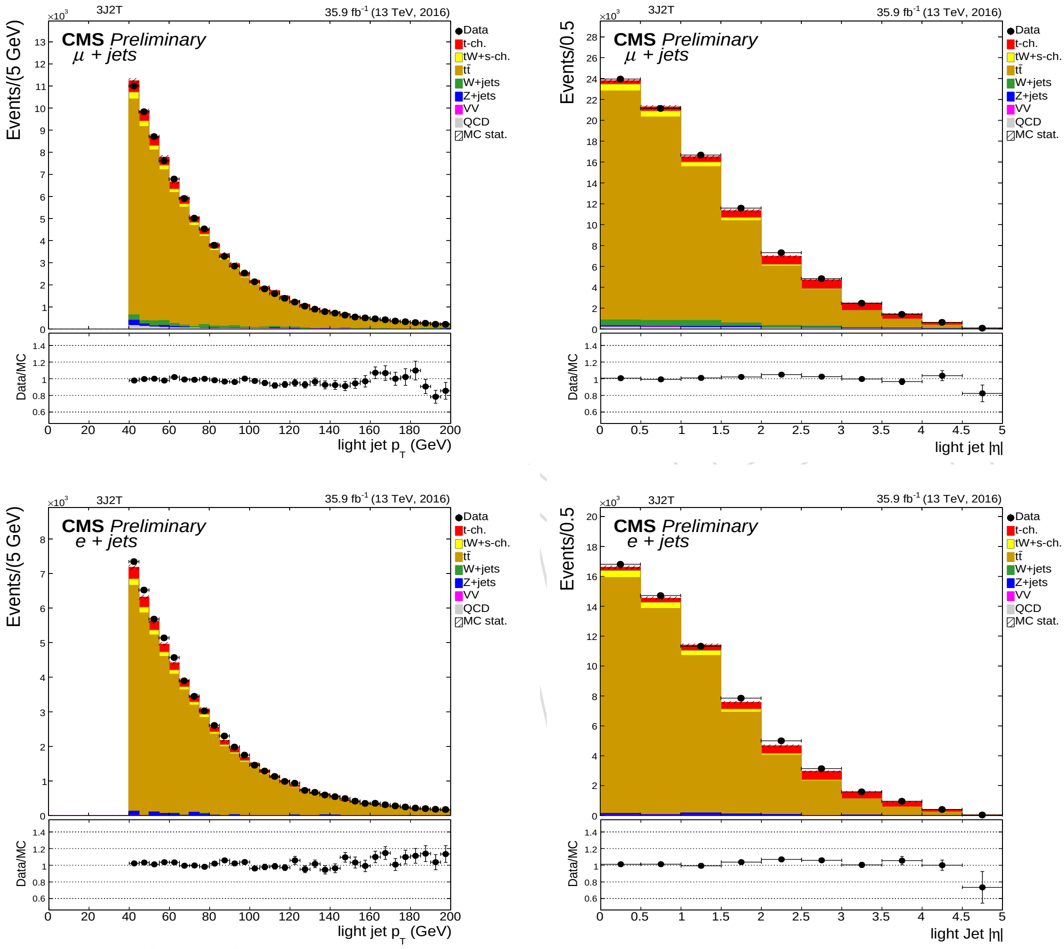

Figure 17: Data-MC comparison of light-flavor jet p_T (left) and $|\eta|$ (right) corresponding to muon (top) and electron (bottom) final states in 3J2T.

5 Cut Flow

Tables 3 and 4 summarizes the step-by-step event yields for simulated signal and background events as well as in data in the signal-enriched 2J1T region, when the selection criteria are applied sequentially.

Table 3: Cut flow for events with the muon final state.

Cut	*t*-ch.	tW + *s*-ch.	$t\bar{t}$	W+jets	Z+jets	di-boson	QCD	Total MC	Data	Data/MC(%)
No cut	7778510	2922066	2.98178e+07	2.20583e+09	2.06715e+08	2780995	1.08515e+010	13307344371	786809782	5.91
Trigger	522403	431879.5	4.03312e+06	3.09301e+08	4.46127e+07	576838.2	1.56223e+08	515700940.7	469761390	91.09
1 tight isolated μ	406617	331738	2.97164e+06	2.33916e+08	2.28107e+07	434859.5	2.47365e+07	285608054.5	258382120	90.47
Loose μ veto	404505	319712.8	2.84126e+06	2.33563e+08	1.29449e+07	406448.96	2.38424e+07	274322226.76	245109050	89.35
e veto	402917	292559.1	2.56513e+06	2.33386e+08	1.28375e+07	375387.93	2.38121e+07	273671594.03	244545880	89.36
2 jets	151988.9	105039.5	695845	6.60088e+06	590102	81312.9	1.46003e+06	9685198.3	8000147	82.60
1 b-tag	64472.5	39140.78	278100	103099	18926.7	2160.19	150628	656527.18	544798	82.98
$m_T^W > 50$ GeV	44946.6	26523.49	191354	74884.2	9781.65	1407.99	36526.1	385424.04	340453	88.33

Table 4: Cut flow for events with the electron final state.

Cut	*t*-ch.	tW + *s*-ch.	$t\bar{t}$	W+jets	Z+jets	di-boson	QCD	Total MC	Data	Data/MC(%)
No cut	7717690	2924052	30895200	2.17e+09	2.08e+08	2783180	6.41e+11	6.44e+11	843398435	0.1
Trigger	309594	288290.9	2660710	1.42e+08	2.72e+07	353090.5	9.71e+07	2.70e+08	292170629	108.2
1 Tight isolated e	229830.3	220699.3	2019920	8.60e+07	1.42e+07	251417.7	1.21e+07	1.15e+08	117287424	102.0
Loose e veto	229067.5	211554.3	1920620	8.60e+07	5752430	228387.7	1.21e+07	1.06e+08	108316594	101.8
μ veto	227904.9	190603.3	1711180	8.58e+07	5709520	208425.8	1.21e+07	1.06e+08	107856987	101.8
2 Jets	86035.3	68740.7	456275	2929229	529504	48973.8	1356662.3	5475420.1	5918361	108.1
1 b-tag	36664.9	25065.9	182395	49618.5	16016.1	1331.1	28739.4	339830.9	359251	105.7
$\not{p}_T > 30$ GeV	27782.1	19327.2	148045	35952.9	7676.3	966.4	16778.2	256528	260515	101.6

6 Top Quark Reconstruction

The four-momentum of the top quark is calculated from the available kinematic information in an event. The top quark decays to a b-tagged jet, a charged lepton and a neutrino, whose transverse momentum can be inferred from $\not{p}_T$. The longitudinal momentum of the neutrino, $p_{z,\nu}$, is determined from the kinematic constraint, namely the W boson mass, $m_W = 80.4$ GeV [40]. Assuming energy-momentum conservation at the W$\rightarrow$ $\mu\nu$ vertex, one can obtain the expression for $p_{z,\nu}$ as:

$$p_{z,\nu} = \frac{\Lambda\, p_{z,\ell}}{p_{T,\ell}^2} \pm \frac{1}{p_{T,\ell}^2}\sqrt{\Lambda^2 p_{z,\ell}^2 - p_{T,\ell}^2(E_\ell^2 \not{p}_T^2 - \Lambda^2)}, \text{where } \Lambda = \frac{m_W^2}{2} + \vec{p}_{T,\ell} \cdot \vec{\not{p}}_T \tag{10}$$

Two cases can arise for the solution, as following.

- If the discriminant, i.e., the square root term in Eq.(10), is negative, it leads to complex solutions for $p_{z,\nu}$. In this case, the imaginary part is eliminated by setting m_T^W = m_W, while still respecting the m_W constraint. This sets the discriminant to 0. This condition gives a quadratic relation between $p_{x,\nu}$ and $p_{y,\nu}$ with two possible solutions, and one remaining degree of freedom. The solution corresponding to the minimal distance between $p_{T,\nu}$ and $\not{p}_T$ is chosen.
- For a positive discriminant, the solution corresponding to the smallest absolute value of $p_{z,\nu}$ is chosen [41, 42].

This implies that the four-momentum of the W boson candidate can be completely determined. In the 2J1T and 3J1T regions, the b-tagged jet is assumed to come from the top quark decay. In the 3J1T region, the most forward jet is considered to be the one stemming from the light quark recoiling against the top. In the 3J2T region, the b-tagged jet corresponding to the lowest difference between the reconstructed top quark mass and 172.5 GeV (top quark mass used in simulation for the nominal sample) is attributed to stem from the b-quark from the top decay, while the untagged jet is identified to originate from the light quark. In the 2J0T region, the following three cases are considered.

- If both jets pass b-tagging algorithm, but do not satisfy the tight criterion, then the jet with the higher b-tagging discriminant value is attributed to the b-quark originating from the top.
- If only one of the two jets passes the b-tagging algorithm but does not satisfy the b-tagging discriminator tight criterion, then that jet is identified as the b-jet due to top quark decay.
- In the case where none of the jets pass the b-tagging algorithm, the one with lower $|\eta|$ is assigned as the b-jet from the decay of the top quark.

A detailed study of the jet-to-parton assignment in signal and control regions can be found in Ref. [35]. The four-momentum of the W boson is then added to that of the b-jet candidate to obtain the four-momentum of the mother top quark.

7 QCD Background Estimation

QCD multijet has a huge production cross section in pp collisions. However, only a small fraction of these events can mimic the lepton+jets final state of the applied event selection in this analysis. Thus, the selection efficiency for QCD multijet events is tiny. The large cross section coupled with very small efficiency would require the generation of an extremely large MC sample for this process in order to retain sufficient events surviving our event selection to ensure a reliable description of QCD modeling in the signal region. An alternative and pragmatic way is to define a sideband (SB) in data that is enriched in QCD events and to use the distributions of relevant kinematic variables directly from this region. In the following subsections, the definition of the QCD enriched SB and the estimation of QCD contribution to the signal region (SR) by means of a binned maximum-likelihood (ML) fit are discussed. The m_T^W and $\not{p}_T$ are used as the fit variables for this purpose in the μ+jets and e+jets final states, respectively. As the available QCD statistics is larger in the 2J0T control region, this region has been used as a proof-of-concept of the method, which is later applied to the signal-enriched 2J1T region.

7.1 Modeling and Estimation of QCD Background in 2J0T

The 2J0T control region is dominated by QCD and W+light-flavor jets events. The fraction of QCD events in this region can be significantly increased by inverting the isolation or identification criterion for the muon or electron, e.g., $I_{rel} > 0.2$ or cut-based "veto" identification criteria. Figure 18 shows a comparison between QCD templates in the SR and SB for m_T^W. A good agreement between the two orthogonal regions is observed. Using simulated samples for all relevant signal and background processes, the QCD purity of the SB has been estimated to be $\approx 93\%$. Therefore, small contributions from nonQCD processes in SB can be neglected.
The m_T^W and $\not{p}_T$ variables provide a good discrimination between QCD and nonQCD processes with prompt muons or electrons, respectively in the μ+jets and e+jets events. Therefore, m_T^W

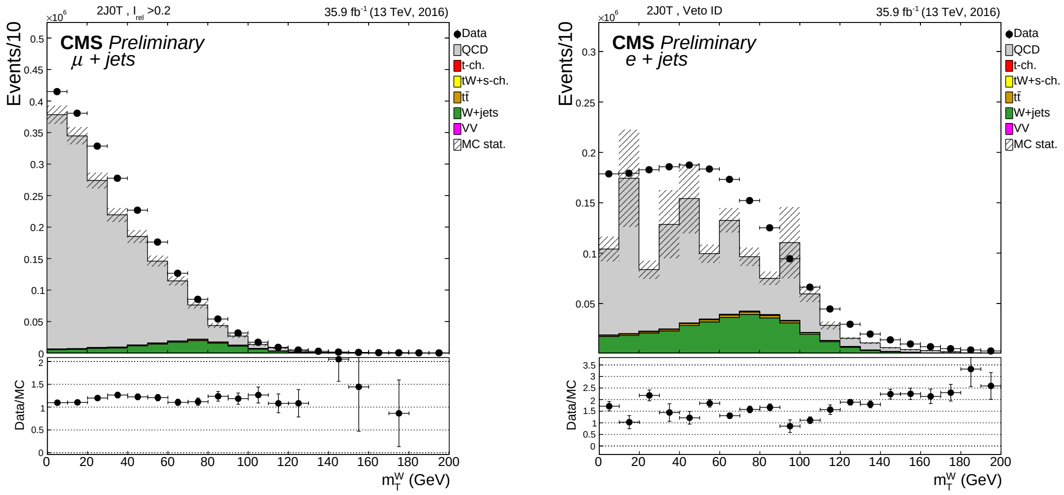

Figure 18: Data-MC comparison for m_T^W in the SB (left) and comparison of the QCD m_T^W templates between SR and SB of 2J0T (right).

($\not{p}_T$) is chosen to be the fit variable, represented by X, in the final state containing muon (electron). A binned extended ML fit with two parameters is performed to the distribution of X in the 2J0T region. We assume that the distribution of X in data, F(X), can be modeled as:

$$F(X) = N_{QCD} \cdot Q(X) + N_{nonQCD} \cdot W(X) \tag{11}$$

where Q(X) stands for the QCD template taken from the SB as described earlier and W(X) represents the combined template for all nonQCD processes obtained by adding up MC contributions of the individual processes in the SR, weighted according to their respective cross sections. Both templates are normalized to an integral of 1.0. The fit parameters N_{QCD} and N_{nonQCD} represent the yields of QCD and nonQCD processes, respectively; they are allowed to float freely during the fit. Figures 19 and 20 show the postfit distributions in μ+jets and e+jets final states, respectively. The fit is repeated with different QCD templates obtained from MC events in SR and SB, as well as a data-driven (DD) template derived in SB by subtracting the contribution of nonQCD processes from data. The entire range of the fit variable distribution is fitted. From the resulting QCD yield, we estimate the QCD contribution in the SR for m_T^W ($\not{p}_T$) $> 50\,(30)$ GeV by calculating the integral of the m_T^W ($\not{p}_T$)-distributions of QCD, normalized to the fit-result, in m_T^W ($\not{p}_T$) $> 50\,(30)$ GeV. The QCD template is derived from data in the SB, as described above, while the actual fit is performed in the SR. The postfit yields with different QCD templates are summarized in Table 5. Overall good agreement, within uncertainties, is observed among results from fits based on different QCD templates, in case of both m_T^W and $\not{p}_T$. The largest difference between the yields for m_T^W ($\not{p}_T$) $> 50\,(30)$ GeV is taken as uncertainty in the QCD normalization for the final state containing muon (electron).

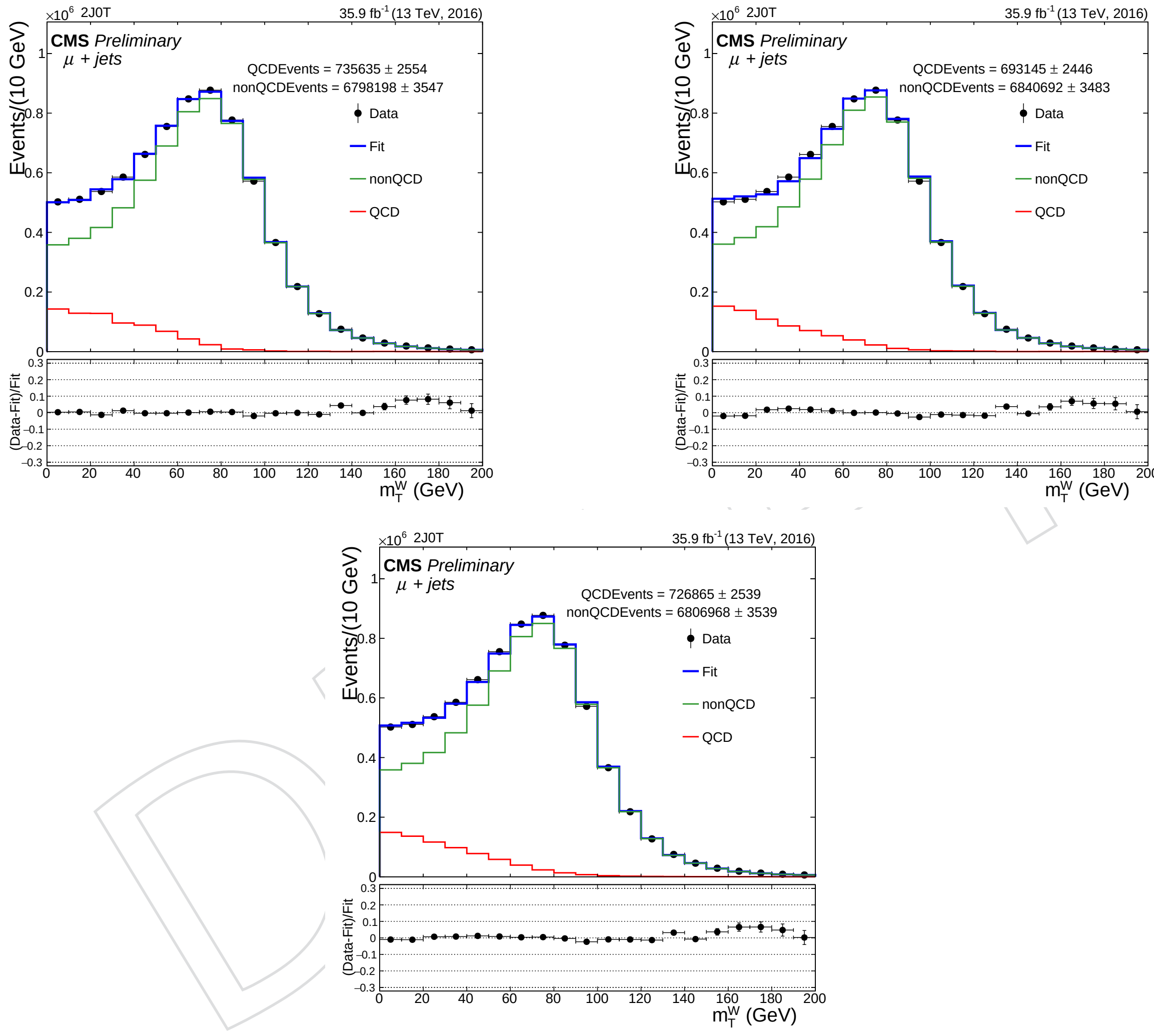

Figure 19: Postfit distribution of m_T^W with different QCD templates: MC templates from SR (top left) and SB (top right), and DD template from SB (bottom).

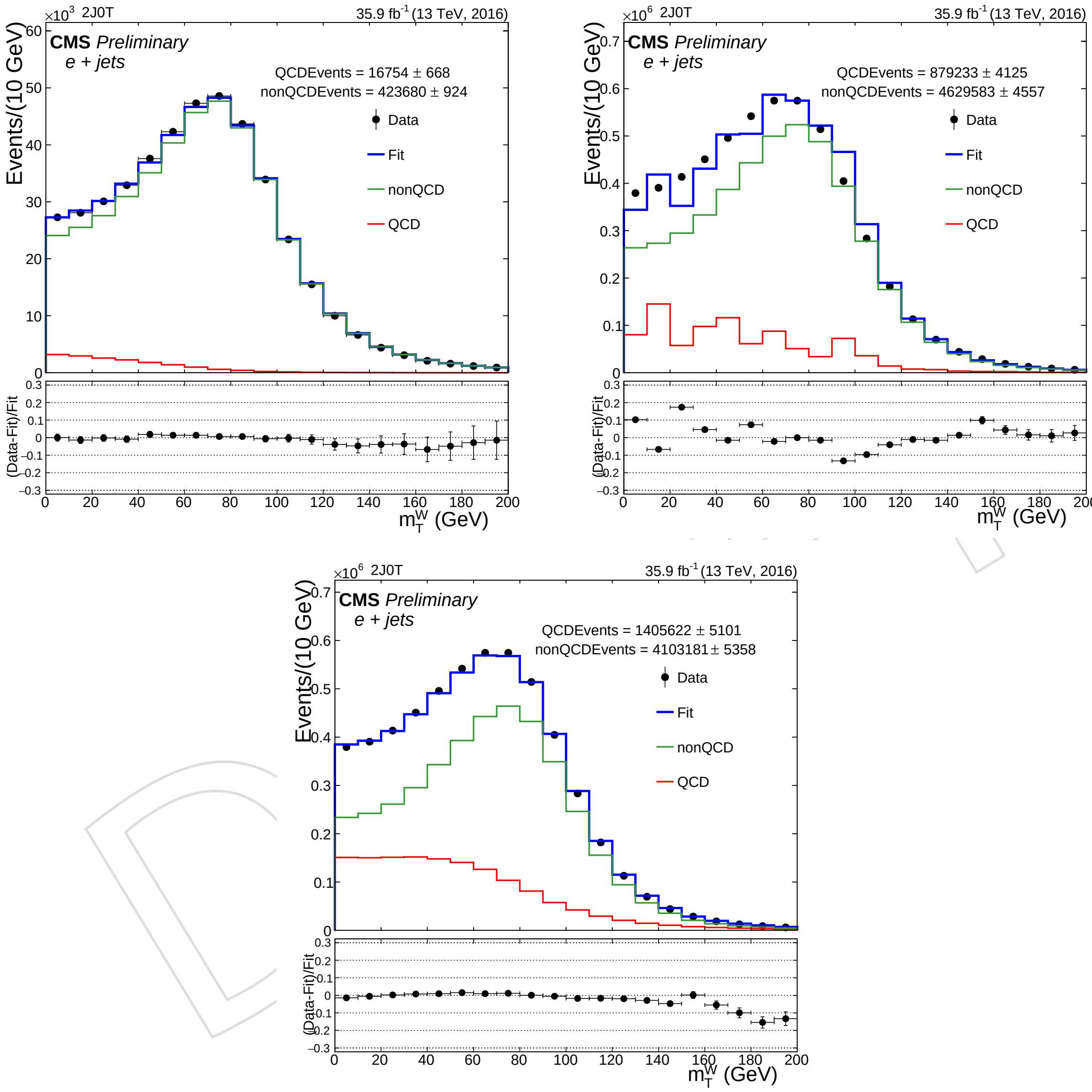

Figure 20: Postfit distribution of m_T^W with different QCD templates: MC template from SR (top left) and SB (top right), and DD template from SB (bottom).

Table 5: QCD estimation in the 2J0T region.

Variable	QCD template	Process	Fitted yield (full range)	Yield for m_T^W ($\not{p}_T$)> 50 (30) GeV
m_T^W	MC template from SB	QCD	635688±2415	122417±465
		nonQCD	6763128±3457	4546640±2324
	Data-driven template from SB	QCD	674599±2538	131951±527
		nonQCD	6724217±3533	4520480±2375
	MC template from SR	QCD	674471±2524	136613±511
		nonQCD	6724343±3524	4520570±2369
$\not{p}_T$	MC template from SB	QCD	1677676±3713	724528±1603
		nonQCD	4732461±4103	3250420±2818
	Data-driven template from SB	QCD	2038996±4340	951068±2024
		nonQCD	4371114±4597	3002240±3157
	MC template from SR	QCD	1813942±3979	815706±1789
		nonQCD	4596206±4314	3156840±2963

7.2 Estimation of QCD Background in 2J1T

7.2.1 Inclusive of lepton charge

The binned ML fit procedure used in the 2J0T control region is applied in the signal-enriched 2J1T region to the fit variable X (X = m_T^W or $\not{p}_T$). The template W(X) is again derived from MC simulation by summing up the individual contributions of different processes, weighted acccording to their respective cross sections, while the QCD template, Q(X), is derived from the SB. Figure 21 shows the data-MC comparison for m_T^W in the SB as well as a comparison of QCD m_T^W-templates from SR and SB in the μ+jets final state.

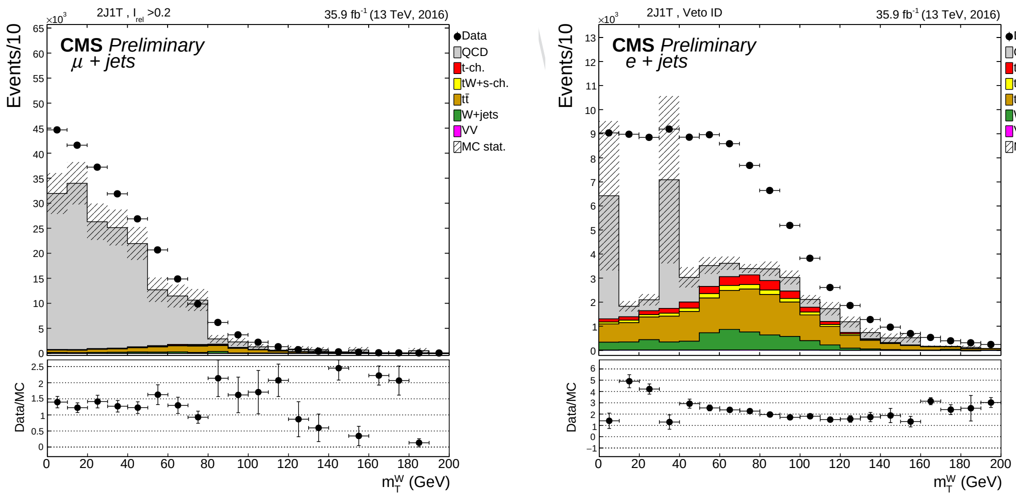

Figure 21: Data-MC comparison for m_T^W in the SB (left) and comparison between the QCD m_T^W-templates derived from SR and SB of 2J1T (right).

As discussed in Section 7.1, the entire m_T^W ($\not{p}_T$)-distribution is fitted and the QCD contribution in the SR for m_T^W ($\not{p}_T$) > 50 (30) GeV is estimated from the postfit m_T^W ($\not{p}_T$)-distribution, normalized to the fit result. Figures 22 and 23 show the postfit distributions for the SR in the μ+jets

Table 6: QCD estimation in the 2J1T region.

Variable	Process	Fitted Yield (full range)	Yield above m_T^W ($\not{p}_T$) $> 50(30)$ GeV
m_T^W	QCD	67928±713	14983±157
	nonQCD	475257±957	322496±649
$\not{p}_T$	QCD	63226±819	31659±410
	nonQCD	293416±949	225532±729

Table 7: QCD estimation in the 2J1T region separated by charge.

	Process	Fitted yield (full range)	Yield for m_T^W ($\not{p}_T$) $> 50(30)$ GeV
μ^+	QCD	32975±511	7217±112
	nonQCD	250244±692	169756±469
μ^-	QCD	34997±496	7778±110
	nonQCD	224971±661	152710±448
e^+	QCD	32109±593	16201±299
	nonQCD	151958±686	116842±528
e^-	QCD	31156±564	15477±280
	nonQCD	141419±655	108661±503

and e+jets final states, respectively. Table 6 reports the postfit QCD and nonQCD yields.

7.2.2 Separation by lepton charge

The same binned ML fit as before is applied to the m_T^W ($\not{p}_T$) distribution in the 2J1T region, but separately for the positively and negatively charged leptons. This is necessary as the final mass measurement will be separately performed for positively and negatively charged leptons. The templates for the nonQCD processes are again derived from MC simulation by summing up the individual contributions from different processes, weighted according to their respective cross sections. The QCD templates are derived from the SB in data, as discussed before. The entire m_T^W ($\not{p}_T$)-distribution in the SR is fitted and the QCD contribution in the SR for m_T^W ($\not{p}_T$) $> 50\,(30)$ GeV is estimated from the postfit m_T^W ($\not{p}_T$)-distributions normalized to the fit result. Table 7 lists the QCD and nonQCD yields obtained from various fits corresponsing to positively and negatively charged leptons. The postfit distributions are shown in Figures 22 and 23 for μ+jets and e+jets final states, respectively.

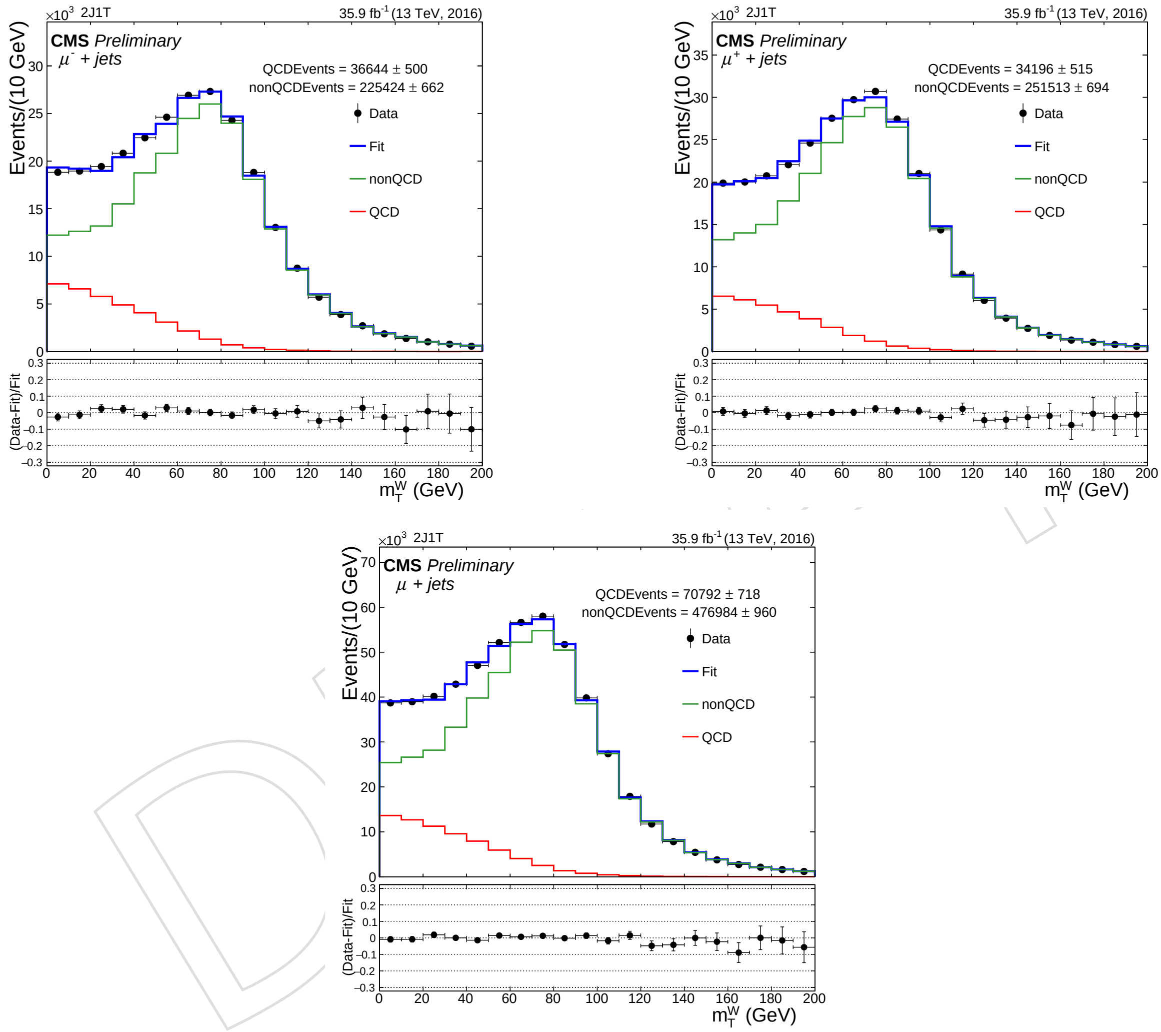

Figure 22: Fit in the SR using data-driven QCD m_T^W template from the SB for μ^- (top left), μ^+ (top right) and inclusive (bottom) cases in the μ+jets final state.

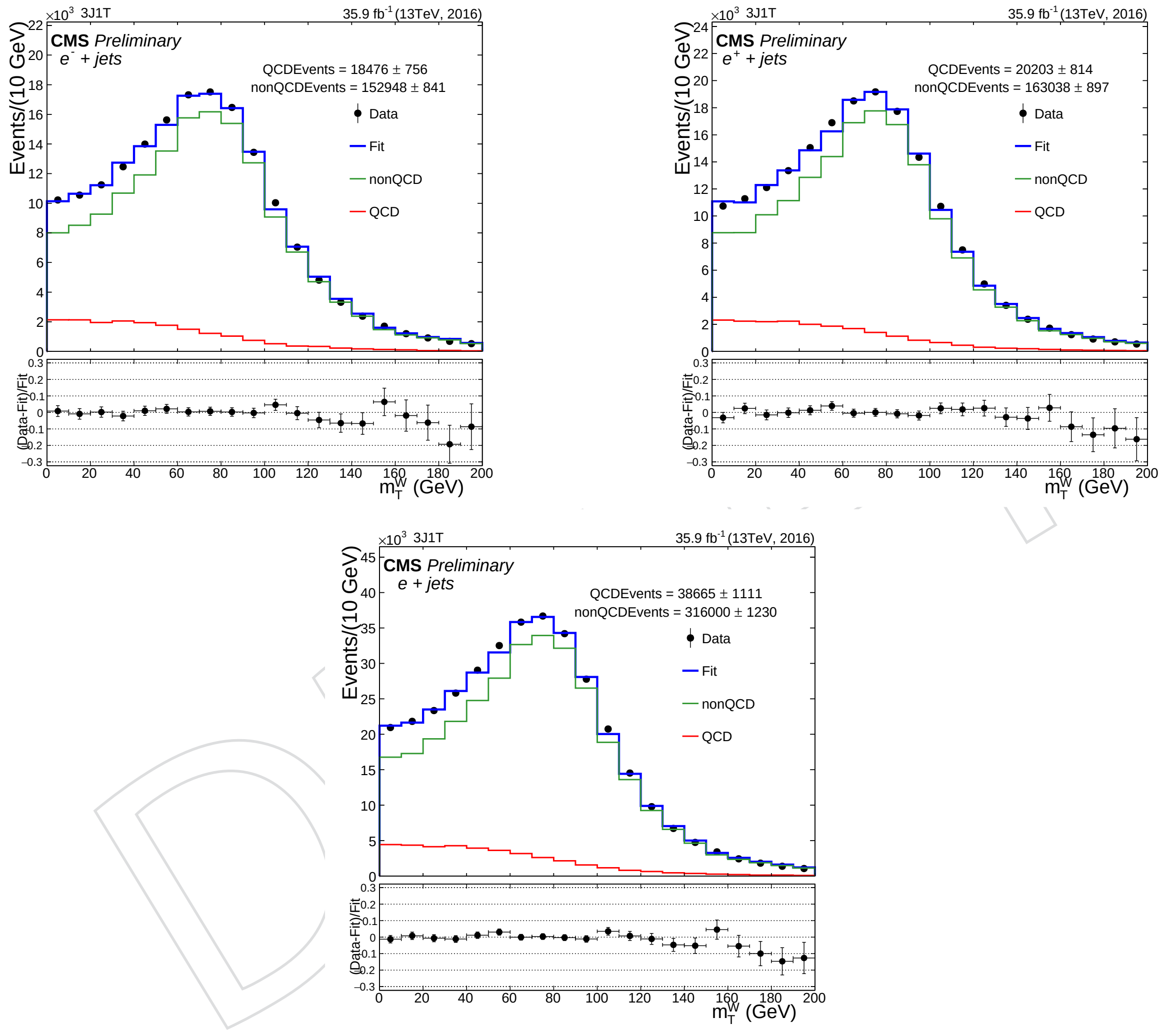

Figure 23: Fit in the SR using data-driven QCD $\not{p}_T$-template from SB region for e^- (top left), e^+ (top right) and inclusive (bottom) cases in the e+jets final state.

8 Multivariate Discriminator

Several input variables can be combined into a single MVA discriminator to achieve a better separation between the signal and backgrounds. The correlations among various input variables can also be taken into account while calculating the discriminator. In this analysis, two separate boosted decision trees (BDTs) are developed using the input variables listed in Tables 8 and 9 for the μ+jets and e+jets final states, respectively. The `TMVA` package [43] built into `ROOT` has been used for this purpose.

Table 8: Input variables to BDT ranked according to their separation power for the muon final state.

Rank	Variable	Separation power
1	ΔR(b-jet, light jet)	2.090e-01
2	light jet $\lvert\eta\rvert$	2.056e-01
3	$m_{bj'}$	1.656e-01
4	$\cos\theta^{*}$	6.769e-02
5	m_T^W (>50 GeV)	4.497e-02
6	$\Delta\eta(\mu$, b-jet)	1.343e-02
7	b-jet p_T + light jet p_T	7.352e-03
8	$\lvert\eta\rvert$ of μ	3.584e-04

Table 9: Input variables to BDT ranked according to their separation power for electron final state.

Rank	Variable	Separation power
1	light jet $\lvert\eta\rvert$	2.045e-01
2	$m_{bj'}$	1.764e-01
3	ΔR(b-jet, light jet)	6.444e-02
4	$\cos\theta^{*}$	2.342e-02
6	b-jet p_T + light jet p_T	1.443e-02
5	$\Delta\eta$(e, b-jet)	4.716e-03
7	$\lvert\eta\rvert$ of e	2.450e-04

All input variables are validated by comparing data and MC distributions. The *t*-channel single top signal is trained against $t\bar{t}$ and electroweak (V+jets and VV, V = W or Z) processes in the 2J1T region with QCD mixed in, after applying the m_T^W ($\not{p}_T$) cut for the muon (electron) final state. During training, signal and background processes are weighted according to their purity in the 2J1T region. The BDT setup is checked for overtraining by dividing the MC samples into two independent subsamples, one for BDT training and the other to evaluate its performance. The result is shown in Figure 24, which depicts no overtraining. The input variables are so chosen that the correlation between the reconstructed m_t and the BDT response is as low as possible in both muon and electron final states. This ensures that any cut on the BDT response minimally impacts the reconstructed m_t distribution. The distributions of the BDT response in data as well as in simulation in the 2J1T region for muon and electron final states are shown in Figure 25.

A cut on the BDT response is applied to select a sample enriched in *t*-chanel single top events. The cut is optimized by studying signal and background efficiencies as well as signal purity of

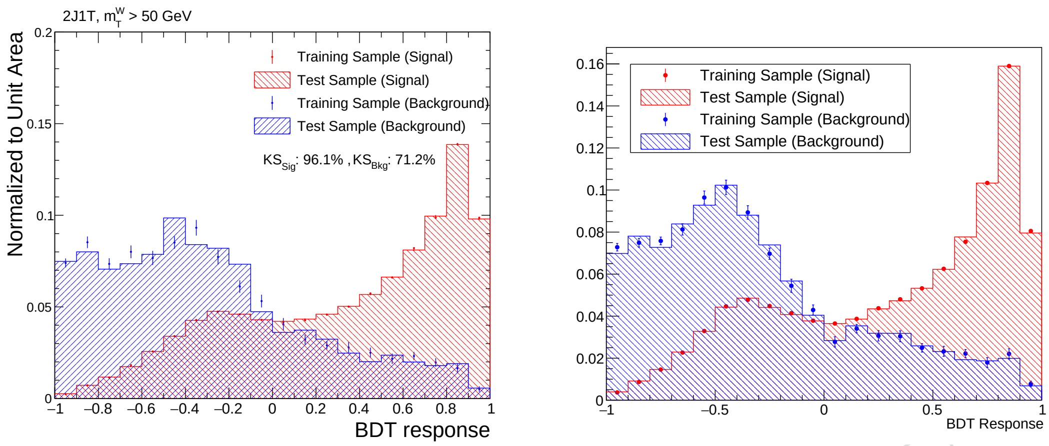

Figure 24: Overtraining check of BDT discriminator between test and training sample for muon (left) and electron (right) final states.

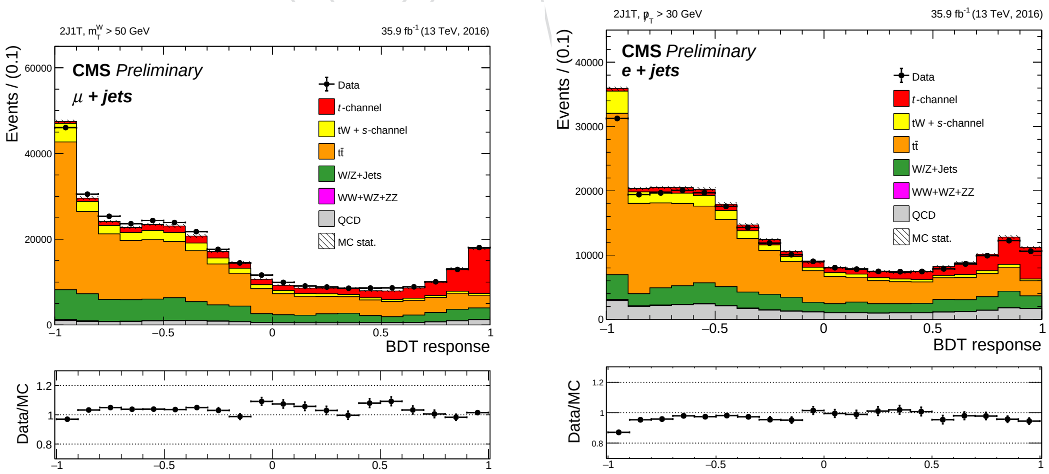

Figure 25: Data-MC comparison of BDT response in 2J1T for muon (left) and electron (right) final states.

the resulting sample after cut, as shown in Figure 27. Based on this study, BDT response > 0.8 is chosen so that the resulting sample has enough signal and background statistics, and more importantly, the cut corresponds to 60.7% (53.1%) signal purity and a signal-to-background ratio of 1.55 (1.13), for the *t*-channel single top process in the muon and electron final states, respectively. The resulting m_t distributions after applying BDT selection are shown in Figure 27.

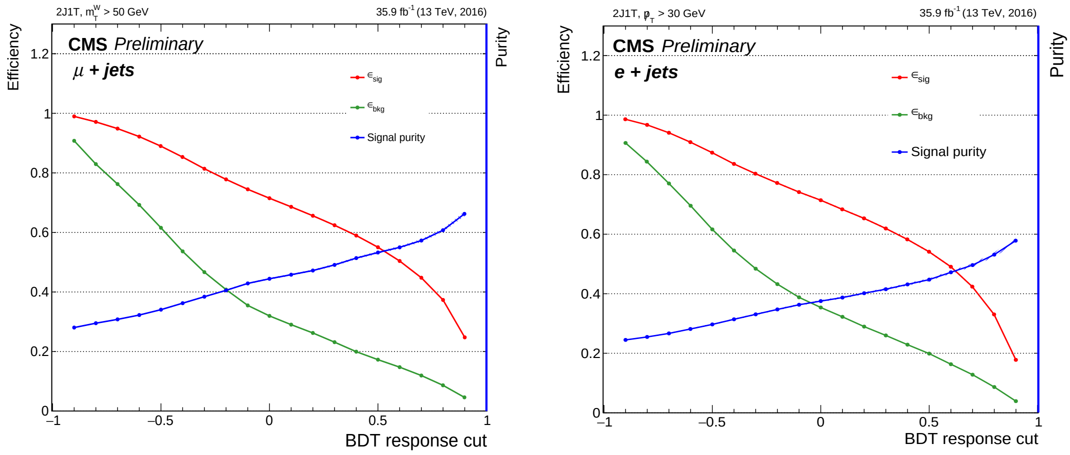

Figure 26: Study of signal and background efficiencies and signal purity as a function of cut on the BDT response for the muon (left) and electron (right) final states.

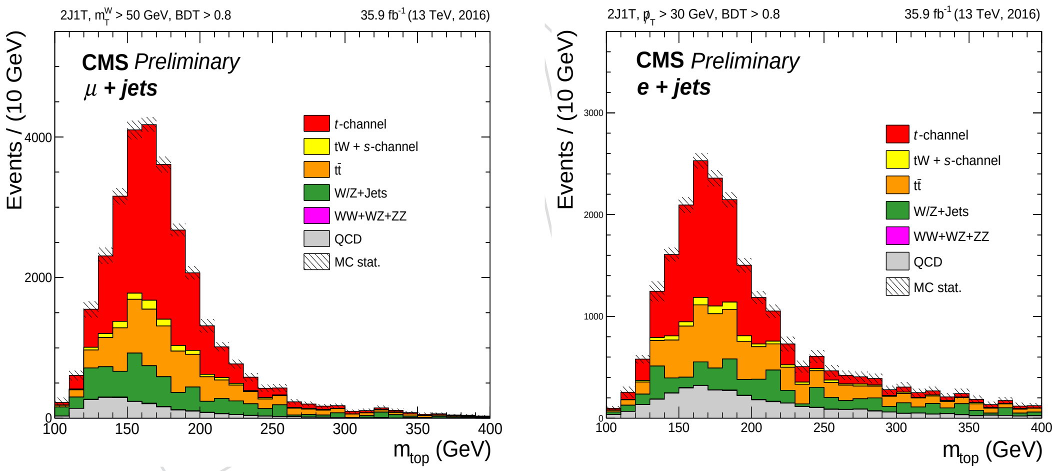

Figure 27: m_t distribution in 2J1T from simulation after applying BDT response > 0.8 for muon (left) and electron (right) final states.

9 Top Mass Extraction

A variety of parametric templates have been tried to model signal and background components in the m_t distribution using the respective MC samples. High skewness of the distribution as well as lower background rate after BDT selection pose a considerable challenge to obtain stable and appropriate parametric templates for both signal and backgrouds. Instead, a suitable alternative is found in the form of the natural logarithm of m_t, i.e., $y = \ln m_t$. It has been observed that, by taking the natural logarithm, the skewness can be significantly reduced [44, 45] for a positive random variable such as m_t, which is skewed to the right. This happens due to the fact that the logarithm *pulls in* more extreme values on the right relative to the mode of the original distribution, whereas the extreme values on left of the mode are *stretched back* farther away from the mode, thus reducing the overall skewness. Also, the logarithm being a monotonic function, the transformed probability density functions are well behaved.
Henceforth, $y = \ln m_t$ distributions from signal and background processes are used for parametric modeling. Figure 28 shows these distributions in simulated events in the 2J1T region after applying the BDT selection. The y distributions obtained from the muon and electron final states are simultaneously considered in the fit. The top quark mass is determined by taking the exponential of the parameter that denotes the peak position (y_0) of the distribution. The parametric 1D template used to simultaneously model in the muon and electron final state can be described as:

$$F(y = \ln\, m_t) = f_{t-ch} \cdot F_{t-ch}(y_0) + f_{Top} \cdot F_{Top}(y_0) + f_{EWK} \cdot F_{EWK}, \tag{12}$$

where F_{t-ch}, F_{Top} and F_{EWK} represent the parametric templates for the signal, top ($t\bar{t}$, tW and *s*-channel) and electroweak (V+jets and VV with V = W or Z) backgrounds, respectively. The signal template, F_{t-ch}, is a sum of an asymmetric Gaussian and Landau functions [46] with unequal peaks. The top background template, F_{Top}, is a Crystal ball function [47] and the electroweak background template,F_{EWK}, is modeled with a Novosibirsk function [48]. The y_0 value of the combined *t*-channel and top background templates along with the normalization scale factor for the *t*-channel single top (f_{t-ch}) process are allowed float during the fit. The normalization scale factors for the top (f_{Top}) and electroweak (f_{EWK}) backgrounds are constrained using log-normal priors with 10% and 30% uncertainties, respectively, to account for uncertainties in the measurement of their respective cross sections at 13 TeV [49–52]. Other shape parameters of the templates comprising the model are tested on simulated samples and each of them is found to agree within a good level of accuracy. Therefore, these shape parameters are kept fixed to the values obtained during nominal fits to the respective MC distributions.
The output of the fit framework behaves linearly as shown in Figure 30 when checked against alternate top mass hypotheses using dedicated signal and $t\bar{t}$ samples. The extracted mass is calibrated with respect to the *true* mass in simulation, and an offset correction is applied to the value obtained from fit to account for the differences between two masses. The deviation of the slope (p1) of the red line shown in Figure 30 from unity can be attributed mostly to resolutions of the b-tagged jet and $\not{p}_T$ which go directly as inputs to the reconstructed m_t. Very little dependence is observed on f_{t-ch} with diffrent top mass hypotheses. Pseudoexperiments are performed to test the robustness of the fit and check for any preset bias in the fit parameters. The respective pull distributions are observed to follow a Gaussian function with mean at zero and unit width, as shown in Figure 31. Pseudoexperiments are also used to determine the expected statistical uncertainty in m_t; its value is obtained to be ± 0.28 GeV.

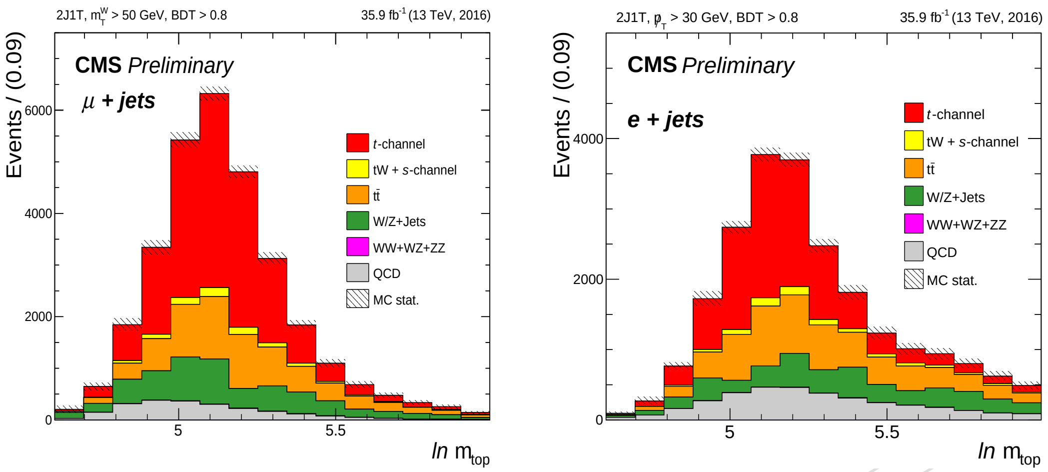

Figure 28: Distribution of $\ln m_t$ after BDT selection in 2J1T using simulated samples for muon (left) and electron (right) final states.

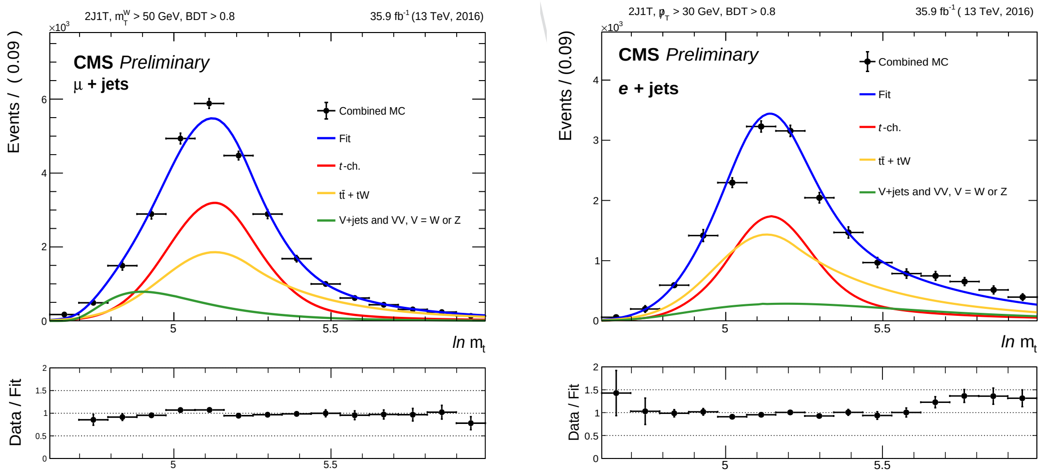

Figure 29: Parametric model for the $\ln m_t$ distribution along with its components in MC events corresponding to muon (left) and electron (right) final states.

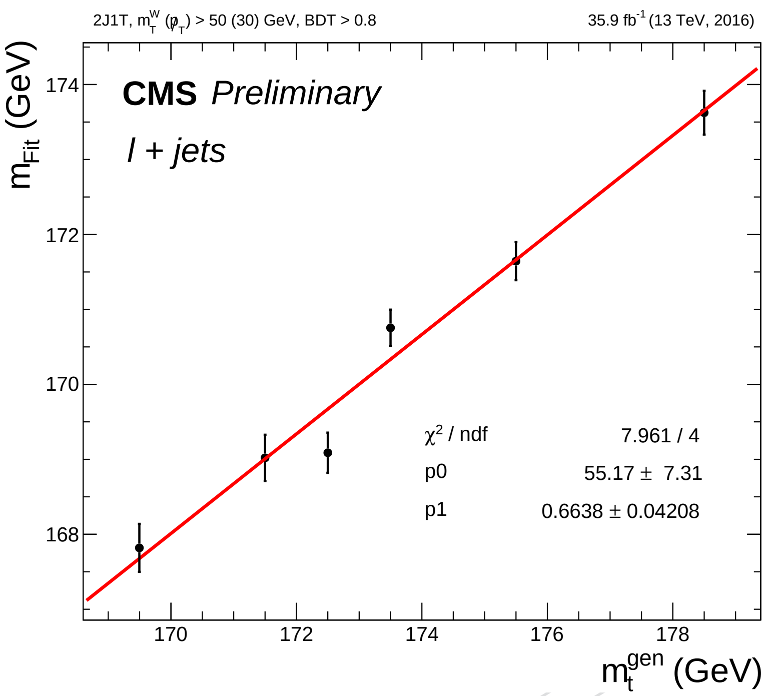

Figure 30: Linearity check of the m_t extracted from fit relative to the true m_t.

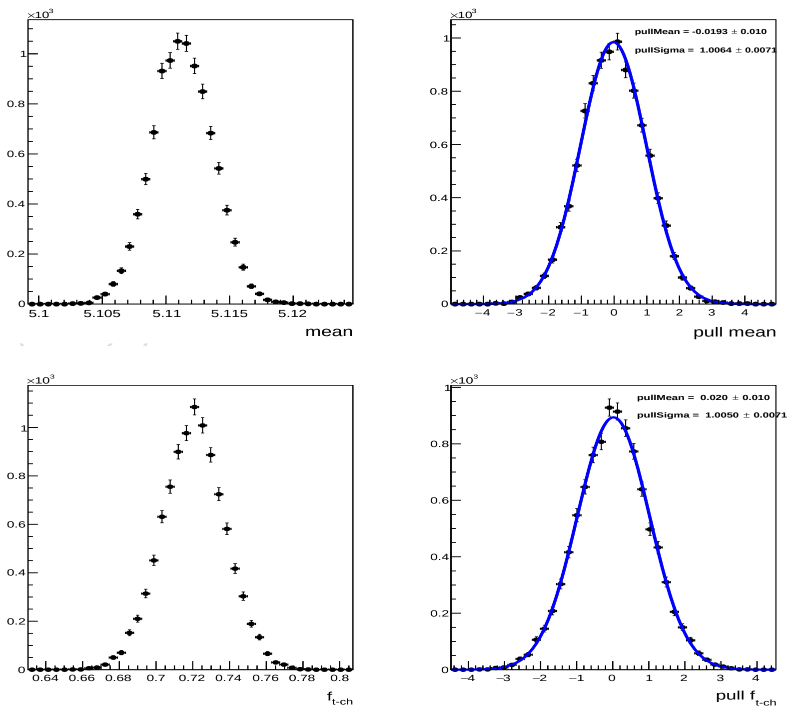

Figure 31: Postfit distribution of fit parameters and their pulls in pseudoexperiments: y_0 (top), f_{t-ch} (bottom).

10 Systematic Uncertainties

Various sources of systematic uncertainty that can affect the measured value of the top-quark mass are considered. Uncertainties are calculated from the difference between the offset-corrected postfit value of m_t corresponding to the nominal and varied templates using pseudoexperiments. The uncertainties can be grouped into two categories, experimental and modeling uncertainties, depending on the nature of systematic source. The impact owing to individual sources are listed in Table 10.

Experimental Uncertainties

- **Jet energy scale:** Energies of all reconstructed jets in simulated events are simultaneously scaled up and down according to their p_T and η-dependent uncertainties [53], split into correlation groups, namely `InterCalibration`, `MPFInSitu` and `Uncorrelated` according to the procedure in Ref. [54]. These variations are also propagated to $\not{p}_T$.
- **Flavor-dependent jet energy corrections:** The Lund string fragmentation implemented in PYTHIA 6.422 [55] is compared to the cluster fragmentation of HERWIG++ 2.4 [56]. Each model relies on a large set of tuning parameters that allow to modify the individual fragmentation of jets initiated from gluons, light and b quarks. Therefore, the difference in jet energy response between PYTHIA 6 and HERWIG++ is determined for each jet flavor [53] and then are added in quadrature.
- **Jet energy resolution:** To account for the difference in the jet energy resolution between data and simulation, a dedicated smearing is applied [53] that increases or decreases the resolutions within their uncertainties.
- **Unclustered energy:** The contributions of unclustered particles to $\not{p}_T$ are varied within their respective energy resolutions [57].
- **Muon and electron efficiencies:** The efficiencies of the lepton identification and isolation, of the used trigger paths as well as of the detector response are determined with a “tag-and-probe” method [58] from Drell-Yan events falling into the Z boson mass window. The uncertainities in the efficiency correction factors are varied in bins of p_T and $|\eta|$.
- **Pileup:** The uncertainty in the average expected number of pileup interactions is propagated as a systematic uncertainty by varying the minimum-bias cross section by $\pm 4.6\%$ [59].
- **b-tagging:** The scale factors used to calculate the efficiency corrections of the cMVAv2 b-tagging algorithm are varied up and down within their uncertainties. From these up and down varied scale factors, up- and down-shifted efficiency corrections are calculated and applied to the simulation.
- **Luminosity:** The relative uncertainty in the integrated luminosity is determined to be $\pm 2.5\%$ [8]. This is propagated as uncertainties in the expected rate of signal and background processes except for QCD, which is determined from data.

Modeling Uncertainties

- **Offset correction:** The offset correction, i.e., the difference between the mass obtained from fit and the true mass is considered to be a function of the mass obtained from fit, using dedicated MC samples with alternate top mass hypotheses(Figure 32). The band about the central line represents ± 1 standard deviation owing to statistical fluctuations of the signal and $t\bar{t}$ samples with different mass hypotheses. The offset correction is obtained from the central value while the corresponding uncertainty is determined from the band and considered as an independent source of uncertainty.

- **Background normalizations:** The contribution of QCD multijet background as estimated by the data-driven method (Section 7) is first subtracted from data. In order to account for the differences in the QCD-estimate using different templates, a $\pm 50\%$ uncertainty in the estimated QCD normalization is considered. The corresponding uncertainty in the measurement is obtained from the difference in fit results due to the the varied templates. The uncertainties $\pm 10\%$ and $\pm 30\%$ in the rates of the top and electroweak backgrounds, respectively, are propagated by considering their rates as nuissance parameters in the fit.
- **Signal modeling:** To determine the influence of possible mismodeling of the signal process, several sources are considered which are listed below.

  Parton shower (PS) scale: The nominal signal sample is compared with dedicated samples generated with a PS scale shifted by ± 1 standard deviation. The uncertainty is estimated from the difference in the fit results due varied samples relative to the nominal one.

  ME/PS matching scale: The model parameter $h_{\mathrm{damp}} = 1.58^{+0.66}_{-0.59}$ (with $\mathrm{m_t} = 172.5$ GeV) [60] used in POWHEG to control the matching of the matrix element to the parton shower (ME-PS matching) and to regulate the high-$\mathrm{p_T}$ radiation in the simulation, is varied within its uncertainties.

  Renormalization/Factorization ($\mu_\mathrm{R}/\mu_\mathrm{F}$) scale: The uncertainties caused by variations in the renormalization and factorization scales ($\mu_\mathrm{R}/\mu_\mathrm{F}$) are considered by applying weights [61], corresponding to simultaneously doubled or halved renormalization and factorization scales with the nominal value set to 172.5 GeV, on the $y = \ln \mathrm{m_t}$ distributions.

  PDF: The impact due to the choice of PDFs is studied using reweighted templates that are derived from all PDF sets of NNPDF 3.0 [62].

- **$\mathrm{t\bar{t}}$ modeling:** The impacts due to variation of the ISR and FSR-PS scales, h_{damp} parameter, $\mu_\mathrm{R}/\mu_\mathrm{F}$ scale and PDF for the $\mathrm{t\bar{t}}$ process are considered by using either dedicated samples or reweighted templates, according to the uncertainty source. The uncertainty is determined from the difference in the fit results obtained from the varied $\mathrm{t\bar{t}}$ templates for each source relative to the nominal one. The contributions from individual sources are summed in quadrature to obtain the total uncertainty due to $\mathrm{t\bar{t}}$ modeling.
- **Electroweak background modeling:** The impacts due to variations of the $\mu_\mathrm{R}/\mu_\mathrm{F}$ scales and PDF for the electroweak processes are considered by using reweighted templates according to the uncertainty source. The impact due to individual sources are again summed in quadrature to obtain the total uncertainty due to electroweak modeling.
- **Top quark $\mathrm{p_T}$:** In differential measurements of the top quark $\mathrm{p_T}$ in $\mathrm{t\bar{t}}$ events, the predicted $\mathrm{p_T}$ spectrum is found to be harder than the observed spectrum [63]. To account for this mismodeling, postfit mass obatined using the default simulation for $\mathrm{t\bar{t}}$ is compared to the one based on simulated $\mathrm{t\bar{t}}$ events that are reweighted according to the observed difference between data and simulation in Ref. [63].
- **Color reconnection Tune:** The uncertainties that arise from ambiguities in modeling color reconnection effects are estimated by comparing among the default model in PYTHIA 8 with two alternative models of color reconnection, one with string for-

mation beyond leading color (QCD inspired) [64] and the other in which the gluons can be moved to another string (gluon move) [5]. In addition, the effects of color reconnection on the top decay products is considered by enabling early resonance decays (ERD) in PYTHIA 8. All models are tuned to measurements of the underlying event [65] and simulataneous variations of different tunes in t-channel single top signal and $t\bar{t}$ are considered. The largest observed shift are quoted as the systematic uncertainty.

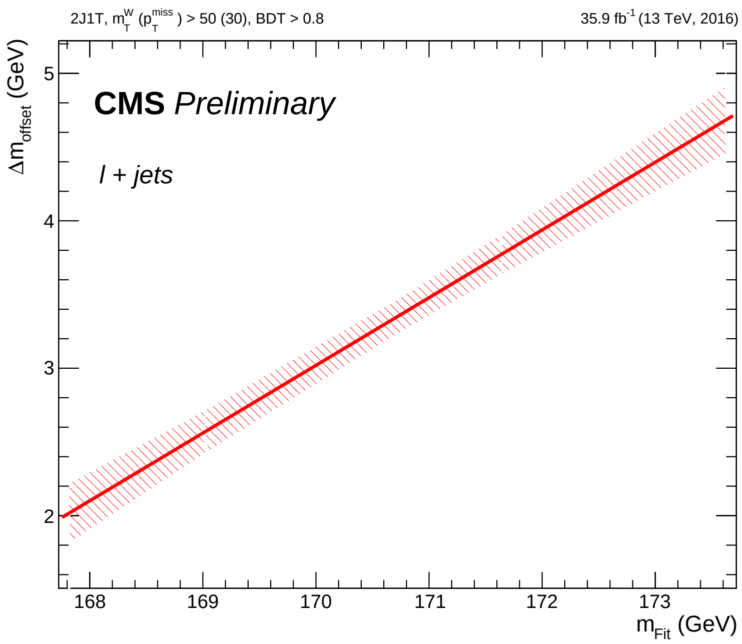

Figure 32: Offset correction as a function of the postfit mass.

Table 10: Summary of systematic uncertainties.

Source		δm (GeV)
muon efficiencies	identification	± 0.01
	isolation	$< \pm 0.01$
	trigger	$< \pm 0.01$
	total	± 0.01
electron efficiencies	identification	± 0.02
	trigger	± 0.03
	total	± 0.04
b-tagging	b-tagging efficiency	± 0.22
	misidentification probability	± 0.03
	total	± 0.22
pileup		± 0.03
offset correction		± 0.14
top p_T reweighting		-0.01
color reconnection tune	″gluon move″ with ERD vs default with ERD	$+0.09$
	″QCD inspired″ vs ″gluon move″	-0.05
		± 0.09
Luminosity		± 0.01
Total syst.		± 0.28
stat. + bkg. norm.		± 0.27
Grand total		± 0.39

11 Results

Based on a blind analysis with MC simulated events having *true* m_t set at 172.5 GeV, the value of the top quark mass measured with single top events in *t*-channel, obtained from the postfit $\ln m_t$ distribution followed by offset correction, is given by:

$$m_t = 172.69 \pm 0.27(\text{stat} + \text{bkg. norm.}) \pm 0.28(\text{syst})\,\text{GeV} = 172.69 \pm 0.39\,\text{GeV} \quad (13)$$

The first uncertainty is due to the combined effect of uncertainties due to statistics and background normalizations, whereas the second denotes the total systematic uncertainty obtained so far. A total uncertainty of 0.39 GeV is obtained by adding the two uncertainties in quadrature.

References

[1] S. Alekhin, A. Djouadi, and S. Moch, "The top quark and Higgs boson masses and the stability of the electroweak vacuum", *Phys. Lett.* **B716** (2012) 214–219, `doi:10.1016/j.physletb.2012.08.024`, `arXiv:1207.0980`.

[2] ATLAS, CDF, CMS, D0 Collaborations, "First combination of Tevatron and LHC measurements of the top-quark mass", `arXiv:1403.4427`.

[3] M. Aliev et al., "HATHOR: HAdronic Top and Heavy quarks crOss section calculatoR", *Comput. Phys. Commun.* **182** (2011) 1034–1046, `doi:10.1016/j.cpc.2010.12.040`, `arXiv:1007.1327`.

[4] P. Kant et al., "HatHor for single top-quark production: Updated predictions and uncertainty estimates for single top-quark production in hadronic collisions", *Comput. Phys. Commun.* **191** (2015) 74–89, `doi:10.1016/j.cpc.2015.02.001`, `arXiv:1406.4403`.

[5] S. Argyropoulos and T. Sjstrand, "Effects of color reconnection on $t\bar{t}$ final states at the LHC", *JHEP* **11** (2014) 043, `doi:10.1007/JHEP11(2014)043`, `arXiv:1407.6653`.

[6] CMS Collaboration, "Measurement of the top quark mass using single top quark events in proton-proton collisions at $\sqrt{s} = 8$ TeV", *Eur. Phys. J.* **C77** (2017) 354, `doi:10.1140/epjc/s10052-017-4912-8`, `arXiv:1703.02530`.

[7] ATLAS Collaboration, "Measurement of the top quark mass in topologies enhanced with single top-quarks produced in the t-channel in $\sqrt{s} = 8$ TeV ATLAS data", Technical Report ATLAS-CONF-2014-055, CERN, Geneva, Sep, 2014.

[8] CMS Collaboration, "CMS Luminosity Measurements for the 2016 Data Taking Period", Technical Report CMS-PAS-LUM-17-001, CERN, Geneva, 2017.

[9] P. Nason, "A New method for combining NLO QCD with shower Monte Carlo algorithms", *JHEP* **11** (2004) 040, `doi:10.1088/1126-6708/2004/11/040`, `arXiv:hep-ph/0409146`.

[10] S. Frixione, P. Nason, and C. Oleari, "Matching NLO QCD computations with Parton Shower simulations: the POWHEG method", *JHEP* **11** (2007) 070, `doi:10.1088/1126-6708/2007/11/070`, `arXiv:0709.2092`.

[11] S. Alioli, P. Nason, C. Oleari, and E. Re, "A general framework for implementing NLO calculations in shower Monte Carlo programs: the POWHEG BOX", *JHEP* **06** (2010) 043, doi:10.1007/JHEP06(2010)043, arXiv:1002.2581.

[12] NNPDF Collaboration, "Parton distributions for the LHC Run II", *JHEP* **04** (2015) 040, doi:10.1007/JHEP04(2015)040, arXiv:1410.8849.

[13] J. Alwall et al., "The automated computation of tree-level and next-to-leading order differential cross sections, and their matching to parton shower simulations", *JHEP* **07** (2014) 079, doi:10.1007/JHEP07(2014)079, arXiv:1405.0301.

[14] R. Frederix and S. Frixione, "Merging meets matching in MC@NLO", *JHEP* **12** (2012) 061, doi:10.1007/JHEP12(2012)061, arXiv:1209.6215.

[15] T. Sjöstrand et al., "An Introduction to PYTHIA 8.2", *Comput. Phys. Commun.* **191** (2015) 159–177, doi:10.1016/j.cpc.2015.01.024, arXiv:1410.3012.

[16] GEANT4 Collaboration, "GEANT4: A Simulation toolkit", *Nucl. Instrum. Meth. A* **506** (2003) 250–303, doi:10.1016/S0168-9002(03)01368-8.

[17] J. Allison et al., "Geant4 developments and applications", *IEEE Transactions on Nuclear Science* **53** (2006) 270–278, doi:10.1109/TNS.2006.869826.

[18] N. Kidonakis, "Differential and total cross sections for top pair and single top production", in *Proceedings, 20th International Workshop on Deep-Inelastic Scattering and Related Subjects (DIS 2012): Bonn, Germany, March 26-30, 2012*, pp. 831–834. 2012. arXiv:1205.3453. doi:10.3204/DESY-PROC-2012-02/251.

[19] CMS Collaboration, "Particle-flow reconstruction and global event description with the CMS detector", *JINST* **12** (2017) P10003, doi:10.1088/1748-0221/12/10/P10003, arXiv:1706.04965.

[20] CMS Collaboration, "Offline Primary Vertex Reconstruction with Deterministic Annealing Clustering", Technical Report CMS-IN-2011-014, CERN, Geneva, Jun, 2011.

[21] "Primary vertex sorting". https://indico.cern.ch/event/369417/contributions/1788757/attachments/734933/1008272/pv-sorting-xpog.pdf.

[22] CMS Collaboration, "Pileup Removal Algorithms", Technical Report CMS-PAS-JME-14-001, CERN, Geneva, 2014.

[23] CMS Collaboration, "Baseline muon selections for Run-II - Muon Identification", 2017. https://twiki.cern.ch/twiki/bin/view/CMS/SWGuideMuonIdRun2#Muon_Identification.

[24] CMS Collaboration, "Cut Based Electron ID for Run 2", 2017. https://twiki.cern.ch/twiki/bin/view/CMS/CutBasedElectronIdentificationRun2.

[25] M. Cacciari, G. P. Salam, and G. Soyez, "The Anti-k(t) jet clustering algorithm", *JHEP* **04** (2008) 063, doi:10.1088/1126-6708/2008/04/063, arXiv:0802.1189.

[26] CMS Collaboration, "Jet Identification", 2016. https://twiki.cern.ch/twiki/bin/viewauth/CMS/JetID.

[27] CMS Collaboration, "Recommended Jet Energy Corrections and Uncertainties For Data and MC", 2017. https://twiki.cern.ch/twiki/bin/view/CMS/JECDataMC.

[28] CMS Collaboration, "Jet Energy Resolution", 2017. https://twiki.cern.ch/twiki/bin/viewauth/CMS/JetResolution#JER_Scaling_factors_and_Uncertai.

[29] CMS Collaboration, "Identification of heavy-flavour jets with the CMS detector in pp collisions at 13 TeV", *JINST* **13** (2018) P05011, doi:10.1088/1748-0221/13/05/P05011, arXiv:1712.07158.

[30] CMS Collaboration, "MET software changes:bad muons and Egamma gain switch fix", 2017. https://indico.cern.ch/event/613987/contributions/2475405/attachments/1413192/2162429/MET_OverviewMuonEGFix_150217.pdf.

[31] CMS Collaboration, "Pileup Reweighting Utilities", 2017. https://twiki.cern.ch/twiki/bin/viewauth/CMS/PileupMCReweightingUtilities.

[32] CMS Collaboration, "Utilities for Accessing Pileup Information for Data", 2017. https://twiki.cern.ch/twiki/bin/view/CMS/PileupJSONFileforData#Pileup_JSON_Files_For_Run_II.

[33] MuonPOG, "Reference muon id, isolation and trigger efficiencies for Run-II", 2017. https://twiki.cern.ch/twiki/bin/view/CMS/MuonReferenceEffsRun2.

[34] MuonPOG, "Muon T&P Instructions for Run-II", 2017. https://twiki.cern.ch/twiki/bin/view/CMS/MuonTagAndProbeTreesRun2.

[35] t-channel working group, "Selection for the single top *t*-channel analyses with the 2016 dataset at 13 TeV", *CMS AN-17-056* (2017).

[36] EgammaPOG, "Instructions for applying electron and photon ID", 2017. https://twiki.cern.ch/twiki/bin/view/CMS/EgammaIDRecipesRun2.

[37] EgammaPOG, "Details of the Tag and Probe procedure for Egamma", 2017. https://twiki.cern.ch/twiki/bin/view/CMS/ElectronScaleFactorsRun2.

[38] CMS Collaboration, "Methods to apply b-tagging efficiency scale factors", 2018. https://twiki.cern.ch/twiki/bin/viewauth/CMS/BTagSFMethods#1a_Event_reweighting_using_scale.

[39] CMS Collaboration, "Usage of b/c Tag Objects for 13 TeV Data in 2016 and 80X MC", 2018. https://twiki.cern.ch/twiki/bin/viewauth/CMS/BtagRecommendation80XReReco.

[40] Particle Data Group, "Review of Particle Physics", *Phys. Rev.* **D98** (2018) 030001, doi:10.1103/PhysRevD.98.030001.

[41] CDF Collaboration, "First Observation of Electroweak Single Top Quark Production", *Phys. Rev. Lett.* **103** (2009) 092002, doi:10.1103/PhysRevLett.103.092002, arXiv:0903.0885.

[42] D0 Collaboration, "Observation of Single Top Quark Production", *Phys. Rev. Lett.* **103** (2009) 092001, doi:10.1103/PhysRevLett.103.092001, arXiv:0903.0850.

[43] A. Hoecker et al., "TMVA: Toolkit for Multivariate Data Analysis", *PoS* **ACAT** (2007) 040, arXiv:physics/0703039.

[44] Belle Collaboration, "Evidence for the decay $B^0 \to K^+K^-\pi^0$", *Phys. Rev.* **D87** (2013) 091101, doi:10.1103/PhysRevD.87.091101, arXiv:1304.5312.

[45] BaBar and Belle Collaborations, "The Physics of the B Factories", *Eur. Phys. J.* **C74** (2014) 3026, doi:10.1140/epjc/s10052-014-3026-9, arXiv:1406.6311.

[46] H. Fanchiotti, C. A. Garcia Canal, and M. Marucho, "The Landau distribution", *Int. J. Mod. Phys.* **C17** (2006) 1461–1476, doi:10.1142/S0129183106009928, arXiv:hep-ph/0305310.

[47] T. Skwarnicki, "A study of the radiative CASCADE transitions between the Upsilon-Prime and Upsilon resonances". PhD thesis, Cracow, INP, 1986.

[48] Belle Collaboration, "A detailed test of the CsI(Tl) calorimeter for BELLE with photon beams of energy between 20-MeV and 5.4-GeV", *Nucl. Instrum. Meth.* **A441** (2000) 401–426, doi:10.1016/S0168-9002(99)00992-4.

[49] CMS Collaboration, "Measurement of the production cross section for single top quarks in association with W bosons in proton-proton collisions at $\sqrt{s} = 13$ TeV", *JHEP* **10** (2018) 117, doi:10.1007/JHEP10(2018)117, arXiv:1805.07399.

[50] CMS Collaboration, "Measurement of differential cross sections for top quark pair production using the lepton+jets final state in proton-proton collisions at 13 TeV", *Phys. Rev. D* **95** (2017) 092001, doi:10.1103/PhysRevD.95.092001, arXiv:1610.04191.

[51] CMS Collaboration, "Measurement of inclusive W and Z boson production cross sections in pp collisions at $\sqrt{s} = 13$ TeV", CMS Physics Analysis Summary CMS-PAS-SMP-15-004, CERN, 2015.

[52] ATLAS Collaboration, "Measurement of $W^{\pm}$ and Z-boson production cross sections in pp collisions at $\sqrt{s} = 13$ TeV with the ATLAS detector", *Phys. Lett. B* **759** (2016) 601–621, doi:10.1016/j.physletb.2016.06.023, arXiv:1603.09222.

[53] CMS Collaboration, "Determination of Jet Energy Calibration and Transverse Momentum Resolution in CMS", *JINST* **6** (2011) P11002, doi:10.1088/1748-0221/6/11/P11002, arXiv:1107.4277.

[54] CMS and ATLAS Collaborations, "Jet energy scale uncertainty correlations between ATLAS and CMS at 8 TeV", Technical Report CMS-PAS-JME-15-001. ATL-PHYS-PUB-2015-049, CERN, Geneva, 2015.

[55] T. Sjöstrand, S. Mrenna, and P. Skands, "PYTHIA 6.4 physics and manual", *JHEP* **05** (2006) 026, doi:10.1088/1126-6708/2006/05/026, arXiv:hep-ph/0603175.

[56] M. Bahr et al., "Herwig++ Physics and Manual", *Eur. Phys. J.* **C58** (2008) 639–707, doi:10.1140/epjc/s10052-008-0798-9, arXiv:0803.0883.

[57] CMS Collaboration, "Performance of the CMS missing transverse momentum reconstruction in pp data at $\sqrt{s}$ = 8 TeV", *JINST* **10** (2015), no. 02, P02006, doi:10.1088/1748-0221/10/02/P02006, arXiv:1411.0511.

[58] CMS Collaboration, "Measurements of Inclusive W and Z Cross Sections in pp Collisions at $\sqrt{s} = 7$ TeV", *JHEP* **01** (2011) 080, doi:10.1007/JHEP01(2011)080, arXiv:1012.2466.

[59] CMS Collaboration, "Measurement of the inelastic proton-proton cross section at $\sqrt{s} = 13$ TeV", *JHEP* **07** (2018) 161, doi:10.1007/JHEP07(2018)161, arXiv:1802.02613.

[60] CMS Collaboration, "Investigations of the impact of the parton shower tuning in Pythia 8 in the modelling of $t\bar{t}$ at $\sqrt{s} = 8$ and 13 TeV", Technical Report CMS-PAS-TOP-16-021, CERN, Geneva, 2016.

[61] A. Kalogeropoulos and J. Alwall, "The SysCalc code: A tool to derive theoretical systematic uncertainties", arXiv:1801.08401.

[62] M. Botje et al., "The PDF4LHC Working Group Interim Recommendations", arXiv:1101.0538.

[63] CMS Collaboration, "Measurement of the differential cross section for top quark pair production in pp collisions at $\sqrt{s} = 8$ TeV", *Eur. Phys. J. C* **75** (2015) 542, doi:10.1140/epjc/s10052-015-3709-x, arXiv:1505.04480.

[64] J. R. Christiansen and P. Z. Skands, "String Formation Beyond Leading Colour", *JHEP* **08** (2015) 003, doi:10.1007/JHEP08(2015)003, arXiv:1505.01681.

[65] CMS Collaboration, "Study of the underlying event in top quark pair production in pp collisions at 13 TeV", *Eur. Phys. J.* **C79** (2019) 123, doi:10.1140/epjc/s10052-019-6620-z, arXiv:1807.02810.

A Systematic Samples

Table 11: List of signal and background systematics samples.

Process	$\sigma(\times BR)$[pb]	Dataset name	N_{events}
t-channel,top, hdamp up/down	136.02	ST_t-channel_top_4f_hdampup_inclusiveDecays_13TeV-powhegV2-madspin-pythia8	6000000
		ST_t-channel_top_4f_hdampdown_inclusiveDecays_13TeV-powhegV2-madspin-pythia8	6000000
t-channel, anti-top, hdamp up/down	80.95	ST_t-channel_antitop_4f_hdampup_inclusiveDecays_13TeV-powhegV2-madspin-pythia8	4000000
		ST_t-channel_antitop_4f_hdampdown_inclusiveDecays_13TeV-powhegV2-madspin-pythia8	3999346
t-channel,top, PS-scale up/down	136.02	ST_t-channel_top_4f_scaleup_inclusiveDecays_13TeV-powhegV2-madspin-pythia8	5709148
		ST_t-channel_top_4f_scaledown_inclusiveDecays_13TeV-powhegV2-madspin-pythia8	5946672
t-channel, anti-top, PS-scale up/down	80.95	ST_t-channel_antitop_4f_scaleup_inclusiveDecays_13TeV-powhegV2-madspin-pythia8	3970546
		ST_t-channel_antitop_4f_scaledown_inclusiveDecays_13TeV-powhegV2-madspin-pythia8	3894778
tW-channel, top, PS-scale up/down	35.6	ST_tW_top_5f_scaleup_inclusiveDecays_13TeV-powheg-pythia8_TuneCUETP8M1	997880
		ST_tW_top_5f_scaledown_inclusiveDecays_13TeV-powheg-pythia8_TuneCUETP8M1	993640
tW-channel, anti-top, PS-scale up/down	35.6	ST_tW_antitop_5f_scaleup_inclusiveDecays_13TeV-powheg-pythia8_TuneCUETP8M1	1000000
		ST_tW_antitop_5f_scaleup_inclusiveDecays_13TeV-powheg-pythia8_TuneCUETP8M1	999068
$t\bar{t}$, FSR up/down	831.76	TT_TuneCUETP8M2T4_13TeV-powheg-fsrup-pythia8	56168970
		TT_TuneCUETP8M2T4_13TeV-powheg-fsrdown-pythia8	29636416
$t\bar{t}$, ISR up/down	831.76	TT_TuneCUETP8M2T4_13TeV-powheg-isrup-pythia8	29938880
		TT_TuneCUETP8M2T4_13TeV-powheg-isrdown-pythia8	59037234
t-channel, top, alternate mass	136.02	ST_t-channel_top_4f_mtop1695_inclusiveDecays_13TeV-powhegV2-madspin-pythia8	5802500
		ST_t-channel_top_4f_mtop1715_inclusiveDecays_13TeV-powhegV2-madspin-pythia8	5839700
		ST_t-channel_top_4f_mtop1735_inclusiveDecays_13TeV-powhegV2-madspin-pythia8	5930600
		ST_t-channel_top_4f_mtop1755_inclusiveDecays_13TeV-powhegV2-madspin-pythia8	5930600
		ST_t-channel_top_4f_mtop1785_inclusiveDecays_13TeV-powhegV2-madspin-pythia8	6084480
t-channel, anti-top, alternate mass	80.95	ST_t-channel_antitop_4f_mtop1695_inclusiveDecays_13TeV-powhegV2-madspin-pythia8	3891200
		ST_t-channel_antitop_4f_mtop1715_inclusiveDecays_13TeV-powhegV2-madspin-pythia8	3948000
		ST_t-channel_antitop_4f_mtop1735_inclusiveDecays_13TeV-powhegV2-madspin-pythia8	3927600
		ST_t-channel_antitop_4f_mtop1755_inclusiveDecays_13TeV-powhegV2-madspin-pythia8	3962100
		ST_t-channel_antitop_4f_mtop1785_inclusiveDecays_13TeV-powhegV2-madspin-pythia8	3917400
$t\bar{t}$, alternate mass	831.76	TT_TuneCUETP8M2T4_mtop1695_13TeV-powheg-pythia8	9954200
		TT_TuneCUETP8M2T4_mtop1715_13TeV-powheg-pythia8	19578812
		TT_TuneCUETP8M2T4_mtop1735_13TeV-powheg-pythia8	19419050
		TT_TuneCUETP8M2T4_mtop1755_13TeV-powheg-pythia8	29459232
		TT_TuneCUETP8M2T4_mtop1785_13TeV-powheg-pythia8	16377176
t-channel, top, color reconnection tune	136.02	ST_t-channel_top_4f_CRTune_erdON_13TeV-powhegV2-madspin-pythia8	5935400
		ST_t-channel_top_4f_GluonMoveCRTune_13TeV-powhegV2-madspin-pythia8	5931424
		ST_t-channel_top_4f_GluonMoveCRTune_erdON_13TeV-powhegV2-madspin-pythia8	5965500
		ST_t-channel_top_4f_QCDbasedCRTune_erdON_13TeV-powhegV2-madspin-pythia8	5952488
t-channel, anti-top, color reconnection tune	80.95	ST_t-channel_antitop_4f_CRTune_erdON_13TeV-powhegV2-madspin-pythia8	3971999
		ST_t-channel_antitop_4f_GluonMoveCRTune_13TeV-powhegV2-madspin-pythia8	3958536
		ST_t-channel_antitop_4f_GluonMoveCRTune_erdON_13TeV-powhegV2-madspin-pythia8	3934164
		ST_t-channel_antitop_4f_QCDbasedCRTune_erdON_13TeV-powhegV2-madspin-pythia8	3959800
$t\bar{t}$, color reconnection tune	831.76	TT_TuneCUETP8M2T4_erdON_13TeV-powheg-pythia8	29938880
		TT_TuneCUETP8M2T4_GluonMoveCRTune_13TeV-powheg-pythia8	59037234
		TT_TuneCUETP8M2T4_GluonMoveCRTune_erdON_13TeV-powheg-pythia8	56168970
		TT_TuneCUETP8M2T4_QCDbasedCRTune_erdON_13TeV-powheg-pythia8	29636416